



Cite this: *J. Mater. Chem. A*, 2023, **11**, 13353

## Cation disorder dominates the defect chemistry of high-voltage $\text{LiMn}_{1.5}\text{Ni}_{0.5}\text{O}_4$ (LMNO) spinel cathodes†

Jiayi Cen, <sup>ab</sup> Bonan Zhu, <sup>ab</sup> Séan R. Kavanagh, <sup>ac</sup> Alexander G. Squires <sup>ab</sup> and David O. Scanlon <sup>\*ab</sup>

High-voltage spinel  $\text{LiMn}_{1.5}\text{Ni}_{0.5}\text{O}_4$  (LMNO) can exist in a Mn/Ni ordered  $P4_332$  or disordered  $Fd\bar{3}m$  arrangement with a majority of literature studies reporting improved electrochemical performance for the disordered phase. Through modifying synthesis conditions, the Mn/Ni ordering can be tuned, however oxygen and  $\text{Mn}^{3+}$  stoichiometries are also affected, making it difficult to decouple these responses and optimise performance. Here, we investigate all intrinsic defects in  $P4_332$  LMNO under various growth conditions, using density functional theory (DFT) calculations. We find that the majority of defects are deep and associated with small polarons ( $\text{Mn}^{3+}$ ,  $\text{Mn}^{2+}$  and  $\text{Ni}^{3+}$ ) formation. The tendency for cation disorder can be explained by the low formation energy of the antisite defects and their stoichiometric complexes. The intrinsic Fermi level of LMNO varies from moderately n-type under oxygen-poor conditions to weakly p-type under oxygen-rich conditions. Our work explains experimental observations (e.g. the Mn/Ni disorder) and provides guidelines for defect-controlled synthesis.

Received 30th January 2023  
Accepted 12th April 2023

DOI: 10.1039/d3ta00532a  
[rsc.li/materials-a](http://rsc.li/materials-a)

## Introduction

High-voltage spinel  $\text{LiMn}_{1.5}\text{Ni}_{0.5}\text{O}_4$  (LMNO) is a promising cobalt-free cathode material which can deliver high energy density ( $650 \text{ W h kg}^{-1}$ ) due to its high operating voltage  $\sim 4.7 \text{ V}$  (vs.  $\text{Li}^+/\text{Li}$ ) arising from the  $\text{Ni}^{2+}/\text{Ni}^{4+}$  couple.<sup>1</sup> As an important derivative of the extensively studied  $\text{LiMn}_2\text{O}_4$  mixed-valence spinel (LMO), LMNO has structural and chemical similarities with LMO.<sup>2–4</sup> In both structures  $\text{Li}^+$  occupy tetrahedral ( $\text{T}_d$ ) sites, and the transition metals (TM) occupy octahedral ( $\text{O}_h$ ) sites of the cubic close-packed oxygen arrays. In addition, they have 3D diffusion channels where  $\text{Li}^+$  migrate through “gate sites”: six-member cation rings perpendicular to the diffusion path.<sup>5</sup> LMNO, however, has improved energy density and cycling stability compared to LMO partly due to a reduced prevalence of  $\text{Mn}^{3+}$  in LMNO.  $\text{Mn}^{3+}$  gives rise to pronounced Jahn-Teller (JT) distortion and Mn dissolution *via* disproportionation reactions ( $2\text{Mn}^{3+} \rightarrow \text{Mn}^{2+} + \text{Mn}^{4+}$ ) leading to structural instability.<sup>2,6–8</sup>

Depending on synthesis conditions, LMNO can show site disorder in the octahedral TM cation sites (see Fig. 1).<sup>9</sup> A lower

synthesis/anneal temperature ( $\sim 700 \text{ }^\circ\text{C}$ ) leads to the formation of the ordered ( $P4_332$ ) phase, where Ni and Mn are located at 4b and 12d Wyckoff sites.<sup>10–12</sup> In the ideal  $P4_332$  LMNO, all Mn species present as redox-inactive  $\text{Mn}^{4+}$ . The  $\text{Ni}^{2+}/\text{Ni}^{4+}$  couple gives rise to a distinctive voltage at  $\sim 4.7 \text{ V}$ .<sup>4</sup> Higher synthesis temperatures ( $>700 \text{ }^\circ\text{C}$ ) promote the formation of the  $Fd\bar{3}m$  LMNO with Mn and Ni disordered across the 16d sites. High temperature synthesis may also drive oxygen vacancy formation, which is expected to be compensated by the reduction of  $\text{Mn}^{4+}$  to  $\text{Mn}^{3+}$ , leading to an off-stoichiometric composition ( $\text{LiMn}_{1.5}\text{Ni}_{0.5}\text{O}_{4-\delta}$ ) with the formation of rock-salt phase (e.g.  $\text{Li}_x\text{Ni}_{1-x}\text{O}$ ) impurities.<sup>11,13</sup>  $\text{Mn}^{3+}$  is redox active and the  $\text{Mn}^{3+}/\text{Mn}^{4+}$  redox reaction introduces an additional plateau at  $\sim 4 \text{ V}$  on the voltage profile.<sup>4</sup> The disordered phase generally exhibits better cycling stability and rate capability than the ordered phase, however the connection between disorder and performance has remained unclear, with increasing attention placed on understanding the role of cation disorder.<sup>14–22</sup>

While some studies found that Mn/Ni disorder increases with oxygen vacancy and  $\text{Mn}^{3+}$  formation, others have suggested that the “disordered” phase from different studies is likely to be samples with partial cation disordering, a varying degree of oxygen content and impurity phases.<sup>13,19,20,23–25</sup> Regardless, the correlation between cation disorder and oxygen content has made it difficult to distinguish the key driving factor for improved performance, illustrating the need to decouple these effects and study their impacts independently.

Density functional theory (DFT) is a key tool for studying the defect chemistry of functional materials.<sup>26,27</sup> Previous defect

<sup>a</sup>Department of Chemistry and Thomas Young Centre, University College London, 20 Gordon Street, London WC1H 0AJ, UK. E-mail: [d.scanlon@ucl.ac.uk](mailto:d.scanlon@ucl.ac.uk)

<sup>b</sup>The Faraday Institution, Quad One, Harwell Science and Innovation Campus, Didcot OX11 0RA, UK

<sup>c</sup>Department of Materials and Thomas Young Centre, Imperial College London, Exhibition Road, London SW7 2AZ, UK

† Electronic supplementary information (ESI) available. See DOI: <https://doi.org/10.1039/d3ta00532a>

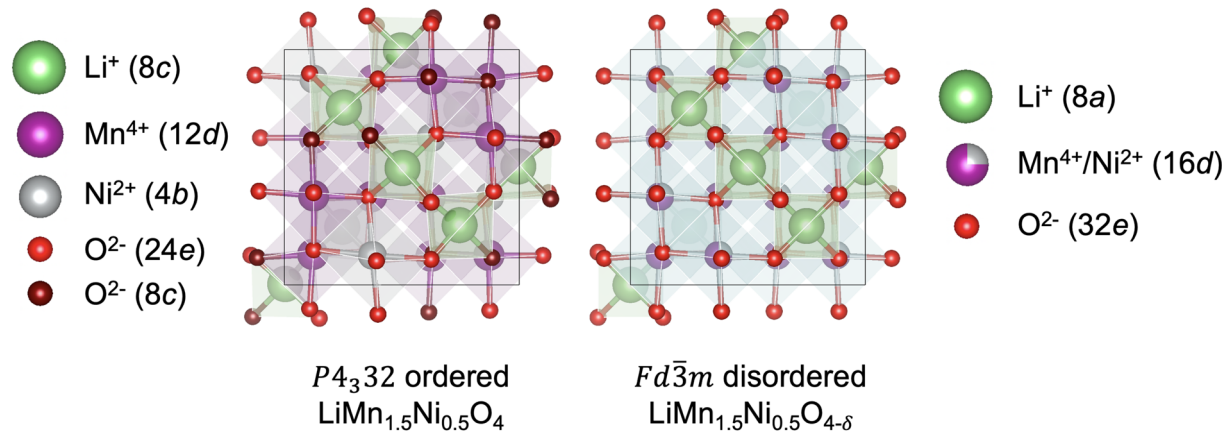


Fig. 1 Representative structures (with Wyckoff positions) of the  $P4_32$  ordered and  $Fd\bar{3}m$  disordered LMNO.

studies<sup>17,24,28–30</sup> have focused on understanding the effects of specific defects on the  $P4_32$  and  $Fd\bar{3}m$  LMNO with various Mn/Ni orderings using a 56-atom supercell. The insights obtained at a microscopic level, such as the Madelung potentials and electronic structures, revealed the likely impacts of oxygen vacancies, which can then be used to explain electrochemical behaviours (e.g. voltage changes and ionic conduction) and to propose optimisation strategies. The high formation energies of TM Frenkel defects explain the sluggish TM ordering transition kinetics. Although they have provided useful insights on defect formation and cation disorder, these studies have various deficiencies: (i) ignoring the effect of atomic chemical potentials on the defect formation energies; (ii) neglecting to address the spurious long-range Coulomb interactions between charged defects inherent within the supercell approach; (iii) calculating defect properties within a small supercell corresponding to unrealistically large defect concentrations.<sup>31,32</sup>

In this paper, we present a comprehensive study of the energetics and behaviour of intrinsic defects in  $P4_32$  LMNO. We first systematically study the magnetic ordering in bulk LMNO, before computing bulk properties and all stable competing phases in the Li–Mn–Ni–O chemical space to determine the phase stability region. We then calculate all intrinsic defects in all possible charge states, using Bader charges, charge densities and Madelung site potential analysis to characterise charge compensation mechanisms and identify small polaron formation. We also investigate a range of likely defect complexes and the migration of lithium defects. Finally, we discuss the effect of synthesis conditions on defect chemistry and how this can explain experimental observations and guide defect-controlled synthesis.

## Methodology

### Computational details

Calculations were performed using spin-polarised plane-wave DFT as implemented in the Vienna *ab initio* Simulation Package<sup>33–35</sup> (VASP) code (version 5.4.4). PAW pseudopotentials<sup>36,37</sup> (version PBE\_5.4) of Li\_sv, Mn\_pv, Ni\_pv and O were

used to model the core electrons. Calculations were performed with the GGA(PBEsol) +  $U$  method<sup>38,39</sup> where  $U$  values for d-orbitals of Mn and Ni were set to 3.9 and 6.0 eV, respectively, based on previous literature studies.<sup>40,41</sup> The initial structure of  $P4_32$  LMNO obtained from Materials Project<sup>42</sup> contains 56 atoms in a primitive cell with 8 formula units of  $\text{LiMn}_{1.5}\text{Ni}_{0.5}\text{O}_4$ . The structure was optimised using a plane-wave cutoff of 550 eV and a  $\Gamma$ -centered Monkhorst–Pack<sup>43</sup>  $k$ -point sampling of  $3 \times 3 \times 3$  ( $k$ -point-spacing of  $0.2528 \text{ \AA}^{-1}$ ) following convergence tests with respect to energy cutoff and  $k$ -points. Tolerances of  $10^{-5}$  eV and  $10^{-2}$  eV  $\text{Å}^{-1}$  were applied to electronic and ionic convergence respectively for bulk and defect calculations.

Pymatgen (version 2020.12.31)<sup>44,45</sup> was used to investigate the magnetic ordering of the bulk structure. Additional calculations were performed using the HSE06 hybrid functional<sup>46</sup> on the ferrimagnetic (FiM) ground state<sup>47</sup> LMNO structure ( $\text{Mn} \uparrow \text{Ni} \downarrow$ ) to compare with the PBEsol +  $U$  results. A denser  $\Gamma$ -centered  $4 \times 4 \times 4$   $k$ -point mesh was used to produce the electronic density of states (DOS) and band structure (path from Bradley and Cracknell<sup>48</sup>).<sup>49</sup>

Defect calculations were conducted using the PBEsol +  $U$  functional on a cubic  $2 \times 2 \times 2$  (448-atom) supercell with  $\Gamma$ -only  $k$ -point grid. Performing calculations using hybrid functional would be practically infeasible with our chosen supercell size due to the exorbitant computational cost. More details about our choice of density functional for this study can be found on page S1 and S2 of the ESI document.† The ferrimagnetic spin configuration was initialised for all defects with fixed-volume relaxations.<sup>50</sup> The force tolerance was raised to  $2 \times 10^{-2}$  eV  $\text{Å}^{-1}$  for interstitial defects. Defect calculations set up and analysis were facilitated by DOPED.<sup>51,52</sup> A lean version of the ShakeNBBreak<sup>53</sup> approach was used to aid the location of the ground-state defect structures.<sup>54,55</sup> With access to the ground state and many metastable defect structures, defect configuration landscape can be explored. This is important for magnetic materials, whereby the magnetic moment of defect structure forms an additional dimension of potential energy surface. Defects with incorrect polaronic localisation upon relaxations were found to exist as higher-energy metastable structures

(typically 0.2–3 eV above the ground state). Displacement distributions with standard deviations of 0.02 Å and 0.05 Å were tested on individual defect structures and the lowest energy relaxed structures were taken for further analysis. Climbing-image nudged elastic band (cNEB) method was used to calculate point defect migration barriers.<sup>56,57</sup> All crystal structure diagrams were prepared using VESTA.<sup>58</sup>

### Defect analysis

The formation energy of a defect  $X$  in a charge state  $q$  with respect to the host lattice is calculated using<sup>26,50,59</sup>

$$E^f(X^q) = E_{\text{tot}}(X^q) - E_{\text{tot}}(\text{host}) - \sum_i n_i \mu_i + q(E_{\text{vbm}} + \mu_e) + \Delta^q, \quad (1)$$

where  $E_{\text{tot}}(X^q)$  and  $E_{\text{tot}}(\text{host})$  are the total energies of a defect supercell and the defect-free supercell respectively.  $\mu_i$  is the atomic chemical potential of species  $i$  and  $n_i$  is the number of atoms of species  $i$  which have been added ( $n_i > 0$ ) or removed ( $n_i < 0$ ) to form the defects.  $\mu_e$  is subject to thermodynamic constraints and can be used to describe experimental conditions.  $\mu_e$  is the electronic chemical potential (*i.e.* the Fermi level), referenced to the valence band maximum (VBM) of the host ( $E_{\text{vbm}}$ ).  $\Delta^q$  is a correction term to align the electrostatic potentials of the defect-free and defect supercells and to account for the finite-cell-size effect on the total energies of charged defects.<sup>31,59</sup> The Freysoldt, Neugebauer and Van de Walle (FNV)<sup>32,60</sup> charge correction scheme was used. This involved computing the static dielectric constant ( $\epsilon_0$ ) with contributions from high-frequency electronic/optical ( $\epsilon_{\text{optic}}$ ) and low-frequency lattice/ionic ( $\epsilon_{\text{ionic}}$ ) contributions:  $\epsilon_0 = \epsilon_{\text{optic}} + \epsilon_{\text{ionic}}$ ,<sup>61</sup> (see Tables S1–S3†).

The chemical potential stability limits of LMNO are defined by the equality

$$\mu_{\text{Li}} + 1.5\mu_{\text{Mn}} + 0.5\mu_{\text{Ni}} + 4\mu_{\text{O}} = \Delta H^f(\text{LiMn}_{1.5}\text{Ni}_{0.5}\text{O}_4), \quad (2)$$

where  $\Delta H^f(\text{LiMn}_{1.5}\text{Ni}_{0.5}\text{O}_4)$  is the formation enthalpy of LMNO. The potential formation of Li–Mn–Ni–O competing phases imposes thermodynamic constraints on  $\mu_i$ , namely that the stoichiometric sum of  $\mu_i$  of a competing phase must not be higher than its formation energy.<sup>31,50</sup> For example, to avoid the formation of NiO would require

$$\mu_{\text{Ni}} + \mu_{\text{O}} \leq \Delta H^f(\text{NiO}) \quad (3)$$

to be satisfied.<sup>62,63</sup> The range of Li, Mn, Ni and O chemical potential values where LMNO is thermodynamically stable can therefore be determined in this way using CPLAP.<sup>63,64</sup> The atomic chemical potential diagrams<sup>65,66</sup> for the host was constructed by exploring the stable competing Li–Mn–Ni–O phases in Materials Project (accessed date: 22 Nov 2020). Magnetic compounds were relaxed with the ground state magnetic ordering, according to previous literature studies.<sup>39,67–76</sup> Elemental reference energies were obtained from the constituent elements in their standard states *e.g.* O<sub>2</sub> (g).<sup>77</sup>

In a solid, defects typically occur in multiple charge states with positive/negative charge states involving removal/addition of electrons. The actual position of Fermi level ( $\mu_e$ ) is determined by minimising the system energy under self-consistent charge neutrality condition using py-sc-fermi:<sup>50,78,79</sup>

$$\sum_{X,q} qc(X^q) + n_h - n_e = 0, \quad (4)$$

where the net charge of a system takes into account all defect species ( $X$ ) with charge  $q$ , free electrons ( $n_e$ ) and free holes ( $n_h$ ). The free carrier concentrations are determined according to the Fermi–Dirac distribution function.<sup>80</sup> The concentration  $c$  of a defect (in thermodynamic equilibrium) at temperature  $T$  is related to its formation energy ( $E^f$ ):<sup>50,59</sup>

$$c = N_{\text{states}} \exp\left(\frac{-E^f}{k_B T}\right), \quad (5)$$

where  $N_{\text{states}}$  is the density of available microstates  $N_{\text{states}} = N_{\text{sites}} N_{\text{config}}$ .  $N_{\text{sites}}$  is the number of symmetry-inequivalent sites in the lattice per unit volume where the defect can be incorporated,  $N_{\text{config}}$  is the number of equivalent configurations (*i.e.* degeneracy) and  $k_B$  is the Boltzmann's constant.

Madelung potentials can suggest where ions in a structure are situated in the energy landscape and the likelihood of redox.<sup>81</sup> They are the electrostatic energies by approximating ions as point charges and can be expressed by a sum of pair-wise interactions:  $E_M = \sum_{(i,j)} \frac{z_i z_j}{r_{ij}}$ , where  $z_i$  and  $z_j$  are the formal charges on ion  $i$  and  $j$  respectively and  $r_{ij}$  is the interionic distance. Cations have negative potentials and anions have positive potentials.<sup>82</sup> A higher potential corresponds to a greater attraction to negative charge (and thus electron polaron formation), and a lower potential to positive charge (thus hole polaron formation).

Defect complex calculations involved constructing supercells with two point defects at a range of pair distances (*e.g.* nearest and farthest). We performed defect complex analysis on the lowest energy configurations, which are those with the smallest pair distance. A generalised equation  $R_1 + R_2 \rightleftharpoons P$  was used to represent their formation, where  $R_1$  and  $R_2$  are reactants (isolated defects) and  $P$  is the product (complex). The enthalpy change for the forward reaction

$$\Delta H = E^f(P) - E^f(R_1) - E^f(R_2), \quad (6)$$

was used to approximate complex association energy, where  $E^f(X)$  is the formation energy of a corresponding defect (complex) species  $X$ .

The equilibrium concentration of complexes can be approximated according to the mass-action law<sup>50,83</sup> using

$$c_{AB} = \frac{c_A c_B}{N_{\text{states}}} \exp\left(-\frac{\Delta H}{k_B T}\right), \quad (7)$$

where  $c_A$  and  $c_B$  are concentrations of isolated defects A and B, respectively.

The Gibbs free energy change  $\Delta G$  for complex formation can be calculated following:



$$\Delta G = \Delta H - T\Delta S. \quad (8)$$

The dominant entropic contribution to the free energy of defects is the configurational entropy, given by:

$$S = k_B \ln W = k_B \ln(N_{\text{states}} C_{c_X}), \quad (9)$$

where  $W$  is the number of microstates and is related to the concentration of defect  $X$  ( $c_X$ ) with potential microstates  $N_{\text{states}}$ . Accounting for the reduction in the configurational entropy upon complex association, and employing the assumptions of (i) equal  $N_{\text{states}}$  for point and complex defects and (ii) majority and minority constituent point defects ( $c_B \gg c_A$ ), a high degree of complex association ( $c_{AB} \geq c_A$ ) is expected when the magnitude of the association energy ( $|\Delta H|$ ) is larger than the entropic cost ( $-T\Delta S$ ), approximated by the critical association energy  $\Delta E_{\text{crit}}$ .<sup>83</sup>

$$-T\Delta S \approx \Delta E_{\text{crit}} = k_B T \log\left(\frac{N_{\text{states}}}{c_B}\right). \quad (10)$$

## Results and discussion

### Bulk properties

**Magnetic ordering.** With the presence of open-shell TM cations in the structure, there are many ways to orient the unpaired electrons. Hence, the starting point towards obtaining the bulk properties of LMNO is to find the correct ground state structure. Erroneous magnetic ordering assignment can lead to an increased computational cost, incorrect ground state energy and electronic structure.<sup>84,85</sup> We have considered all possible magnetic orderings in the 56-atom conventional  $P4_332$  LMNO unit cell. Different magnetic initialisations can lead to a spread of DFT energies after geometry relaxations (Fig. S1†). The ground state magnetic ordering was calculated to be FiM with  $Mn \uparrow Ni \downarrow$ , in line with experimental findings.<sup>47</sup>

**Crystal structure.** The ground state FiM structure was optimised with PBEsol +  $U$  and HSE06 methods separately and the calculated (cubic) lattice constants are in good agreement with experimental data (Table 1). The local coordination around Ni shows six oxygens at equal distances of 2.05–2.06 Å. The local Mn coordination is distorted with three inequivalent Mn–O distances and is a consequence of Mn coordinating to two symmetry-inequivalent oxygens in the 24e sites (surrounded by

**Table 1** Structural parameters obtained from PBEsol +  $U$ , HSE06 calculations and from experimental data<sup>9,87</sup>

Theory/Exp	PBEsol + $U$	HSE06	Exp
Lattice constant [Å]	8.17	8.15	8.166(3)
(Ni–O) $\times$ 6 [Å]	2.05	2.06	2.068(2)
(Mn–O) $\times$ 2 [Å]	1.88	1.87	1.870(4)
(Mn–O) $\times$ 2 [Å]	1.91	1.90	1.914(1)
(Mn–O) $\times$ 2 [Å]	1.94	1.93	1.932(4)

2Mn<sup>4+</sup>, Ni<sup>2+</sup> and Li<sup>+</sup>) and 8c sites (surrounded by 3Mn<sup>4+</sup> and Li<sup>+</sup>). This distortion ( $\Delta d_{\text{Mn–O}} = 0.06$  Å) is minor compared to the pronounced JT distortion for Mn<sup>3+</sup> observed in LMO spinel, with  $\Delta d_{\text{Mn–O}} = 0.28$  Å.<sup>86</sup>

**Electronic structure.** Fig. 2 shows the electronic density of states (DOS) using PBEsol +  $U$  and HSE06 functionals. Both functionals indicate that the VBM is dominated by Ni and O states in the spin-down channel and that the CBM is dominated by Mn and O states in the spin-up channel. The VBM has a larger contribution from O 2p states than Ni 3d states, even with HSE06 where the Ni contribution is increased (from 24%–34%) (Table 2). This phenomenon is also observed in other compounds such as LiNiO<sub>2</sub> where oxygens are bonded to late-3d metals with increased crystal-field splitting. This would decrease the tendency towards hole localisation and redox processes are likely to involve Ni–O hybridised bands strong in O character.<sup>59,88</sup> However, on a per-atom basis, the contribution from Ni states is at least two times higher than that of O at VBM. This is consistent with experimental observations where Ni was shown to be redox-active.<sup>1</sup>

The CBM has a greater proportion of Mn 3d states than O 2p states with both functionals. The presence of oxygen character at the CBM suggests polar covalent Mn–O bonding with hybridised states. Since Mn and Ni dominate the CBM and VBM respectively, charge localisation would occur on Mn (for electron polarons) and Ni (for hole polarons). The Mn 3d states in the spin-up channel at the CBM also suggest that Mn would adopt a high-spin configuration when an additional electron is populated to form Mn<sup>3+</sup> (d<sup>4</sup>). Liu *et al.*<sup>89</sup> suggested that the 2p unoccupied states from O is related to the O<sub>2</sub> release phenomena under thermal treatment, the formation of the rock-salt impurity phases Li<sub>x</sub>Ni<sub>1-x</sub>O and high-temperature phase  $Fd\bar{3}m$  LiMn<sub>1.5</sub>Ni<sub>0.5</sub>O<sub>4-δ</sub> where Mn<sup>3+</sup> is also redox-active. Ryoo *et al.*<sup>90</sup> related the bonding characteristics of Mn–O and Ni–O, both hybridised with a similar degree of covalency, to the propensity for cation disordering in LMNO at elevated temperatures. In contrast, cation ordering is strongly preserved in  $P4_332$  LiGe<sub>1.5</sub>Ni<sub>0.5</sub>O<sub>4</sub> despite Ge<sup>4+</sup> having the same ionic radius to Mn<sup>4+</sup>, even at a very high temperature (e.g. 950 °C), due to the contrasting bonding motifs of Ge–O (ionic) and Mn–O (polar covalent).<sup>90</sup>

Fig. S2† shows the electronic band structure and both functionals show weak band dispersion, reflecting strong electron–electron correlations. LMNO is calculated to be a wide-gap semiconductor, with an indirect band gap of 1.76 and 3.17 eV determined using PBEsol +  $U$  and HSE06 functionals, respectively. The hybrid approach, in theory, should give a more reliable prediction of fundamental band gap compared to PBEsol +  $U$ , in which the magnitude of the band gap is influenced by the choice of  $U$  values.<sup>91</sup> There is limited experimental data on the fundamental band gap to compare with the current study, though an optical gap between 1.2–1.3 eV has been reported experimentally.<sup>92,93</sup> The large difference between the fundamental and optical band gaps is likely due to the strong excitonic effects in flat d-band wide gap materials.<sup>94,95</sup>

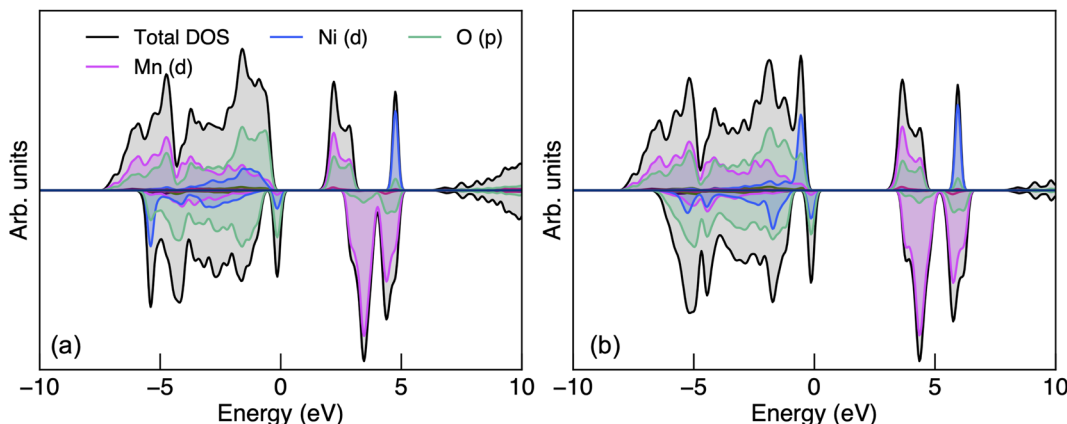


Fig. 2 The electronic density of states of  $P4_332$   $LiMn_{1.5}Ni_{0.5}O_4$  obtained from (a) PBEsol +  $U$  and (b) HSE06 calculations.

Table 2 Percentage of transition metals (Mn and Ni) and oxygen contributions at the valence band maximum (VBM) and conduction band minimum (CBM) in  $P4_332$   $LiMn_{1.5}Ni_{0.5}O_4$  from PBEsol +  $U$  and HSE06 calculations

Theory	PBEsol + $U$		HSE06	
	VBM spin ↓	CBM spin ↑	VBM spin ↓	CBM spin ↑
Spin channel				
O	71%	24%	61%	21%
Ni	24%	0%	34%	0%
Mn	4%	70%	4%	72%

### Phase stability

Thermodynamic stability of LMNO was determined by computing formation energies of all stable competing phases in the Li–Mn–Ni–O phase diagram, where  $Li_2Ni_2O_3$  was obtained using structure prediction.<sup>96</sup> Formation energies of all stable competing phases are summarised in Tables S4 and S5.†

The host material is thermodynamically stable and there are 20 intersection points bounding the stability region in the chemical potential space. Each intersection point corresponds to a facet in the phase diagram where the corresponding phases are in equilibria with the host (see Table S6†). O-rich ( $\mu_O = 0$  eV) oxidizing conditions are usually Mn- and Ni-poor, and favour *p*-type (acceptor) defect formation. O-poor, Mn- and Ni-rich reducing conditions favour n-type behaviour, which can occur under higher temperature and/or reduced oxygen partial pressure and/or under the presence of oxygen-reducing agents (e.g. LiH).<sup>97</sup>

The quaternary phase space of LMNO yields a 4D stability region, thus to allow visualisation on a 2D plot, we show in Fig. 3 the stability region where  $\mu_{Li}$  and  $\mu_{Mn}$  were set to the average values over all atomic chemical potentials intersection points. LMNO is stable across a small  $\mu_{Ni}$  range, a moderate  $\mu_{Li}$  range and a larger  $\mu_{Mn}$  range. The size of the stability field reflects the ease of synthesizing the target product experimentally and determines the range of variation in defect formation energy over all possible growth conditions. Thus, there is

a greater sensitivity of defect concentrations to Mn-related than Ni-related growth environments. The ease of nickel oxide impurity phase formation upon synthesizing LMNO is reflected by the small  $\mu_{Ni}$  window.<sup>12,62</sup>

### Defect structure and energetics

We investigated a range of intrinsic point defects in all possible charge states. This includes all vacancies ( $V_{Li}$ ,  $V_{TM}$  and  $V_O$ ), antisites ( $Li_{TM}$ ,  $TM_{Li}$  and  $TM_{TM}$ ) and interstitials ( $Li_i$ ,  $TM_i$  and  $O_i$ ); 'TM' refers to a transition metal species (Mn or Ni) and vacancies on symmetry inequivalent oxygens in the 24e and 8c sites are denoted by  $V_{O,1}$  and  $V_{O,2}$  respectively. For interstitials, we tested six symmetry inequivalent interstitial positions and their corresponding Wyckoff positions are specified in Table S7.† In addition, the potential formation of peroxide species from oxygen interstitials was tested by placing  $O_i$  at distances  $\sim 1.4$  Å from  $O_{host}$  and relaxing the defect geometry from this structure.<sup>98</sup> We also considered a range defect complexes including the antisite-pair defects ( $Li_{Mn}-Mn_{Li}$ ,  $Li_{Ni}-Ni_{Li}$  and  $Mn_{Ni}-Ni_{Mn}$ ), vacancy-pair (Schottky) defects (e.g.  $V_O-V_{Li}$ ,  $Mn_{Ni}-V_{Li}$ ) and a lithium Frenkel-pair ( $Li_i^+-V_{Li}$ ), due to the low formation energies (and thus high concentrations) of the constituent point defects.

To illustrate the complex nature of defect chemistry of LMNO, in Fig. 4 we have plotted the formation energies of all intrinsic defects in their lowest energy charge states at the self-consistent Fermi levels over the 20 chemical potential conditions from O-rich to O-poor (increasing self-consistent Fermi levels). With the inverse-exponential relationship between defect concentration and formation energy (eqn (5)), the large variation in formation energies across different chemical potentials indicates a strong sensitivity of defect concentrations to growth conditions in LMNO. Transitioning from O-rich to O-poor (A → T), the formation energies of several n-type defects (e.g. oxygen vacancies) decrease sharply (by  $\geq 0.5$  eV). Therefore, the formation of these defects are highly sensitive to the oxygen and/or temperature environments. Formation energies of  $Mn_{Ni}$  and  $Li_{Ni}$  defects remain the lowest in each chemical potential condition, thus the disordering in LMNO is greatly driven by



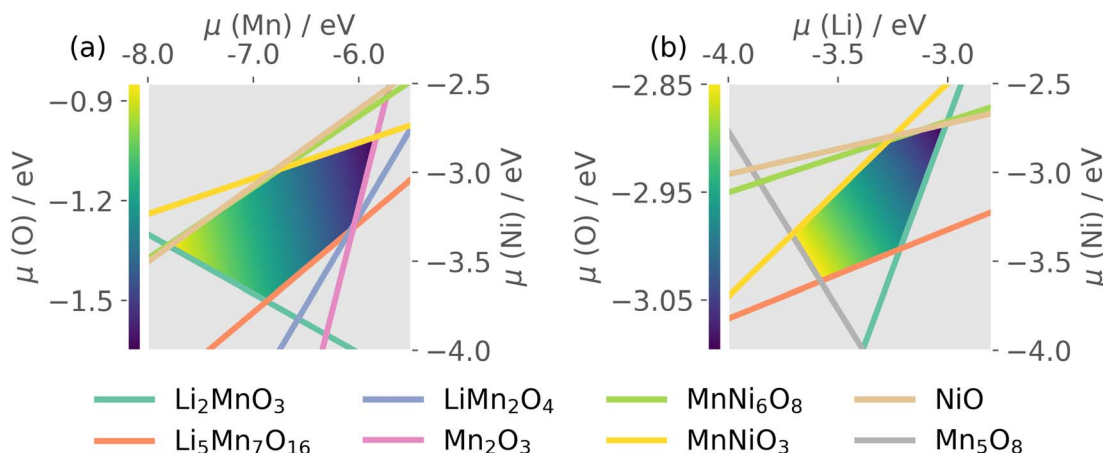


Fig. 3 The chemical potential space of  $P4_332$   $LiMn_{1.5}Ni_{0.5}O_4$ , (a) where chemical potential of Li was set to an average value of  $-3.35$  eV; (b) where chemical potential of Mn was set to an average value of  $-6.42$  eV. Yellow/dark-blue colour shadings represent p/n-type conditions.

those defects. This may also explain typical LMNO samples are not perfectly stoichiometric on the cation sites and are often slightly Ni-deficient  $LiNi_{0.5-x}Mn_{1.5+x}O_4$  ( $x < 0.1$ ).<sup>99</sup>

Fig. 5 shows the defect transition levels under two contrasting conditions A (O-rich; p-type) and T (O-poor; n-type). The

gradient of each line corresponds to defects' charge states. The Fermi level where the formation energy of a defect  $X$  in two charge states  $q_1/q_2$  becomes equal is termed as the thermodynamic transition level  $\varepsilon(q_1/q_2)$  where  $X^{q_1}$  and  $X^{q_2}$  are in thermodynamic equilibrium, and is represented by a filled circle.

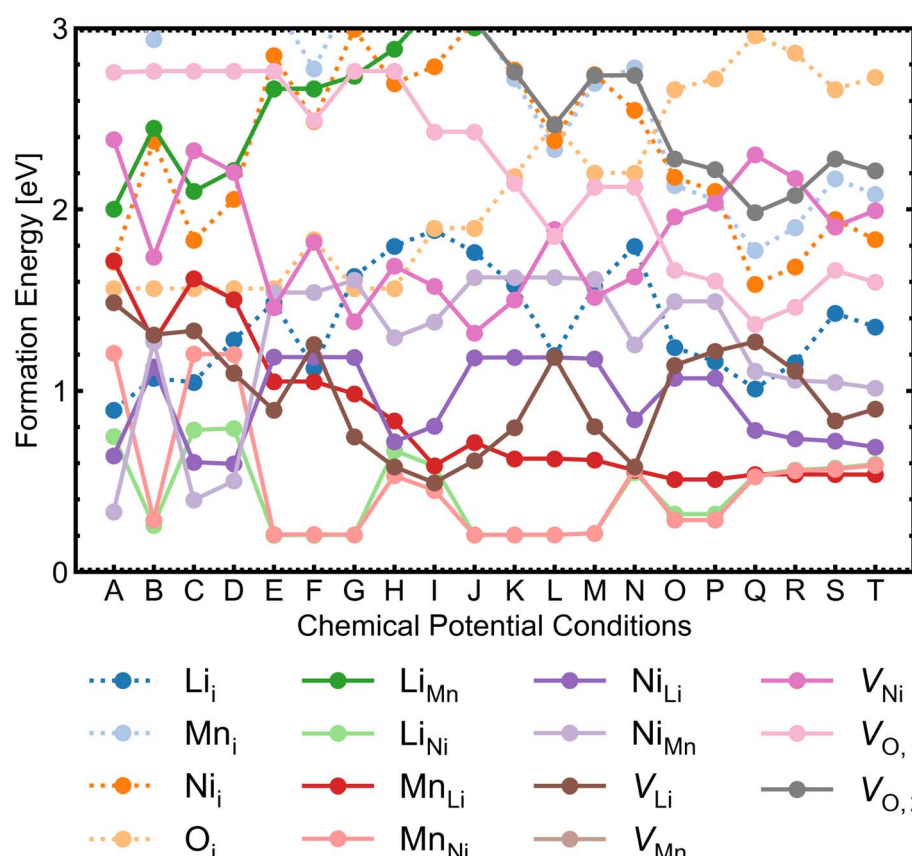


Fig. 4 Formation energies for each intrinsic point defect in the lowest energy charge state at the self-consistent Fermi levels over 20 chemical potential conditions for  $P4_332$   $LiMn_{1.5}Ni_{0.5}O_4$ . The chemical potential conditions (A → T) are arranged in order of increasing self-consistent Fermi level determined from all intrinsic point defects. Interstitial defects are represented by dotted lines; antisite and vacancy defects are shown by solid lines.



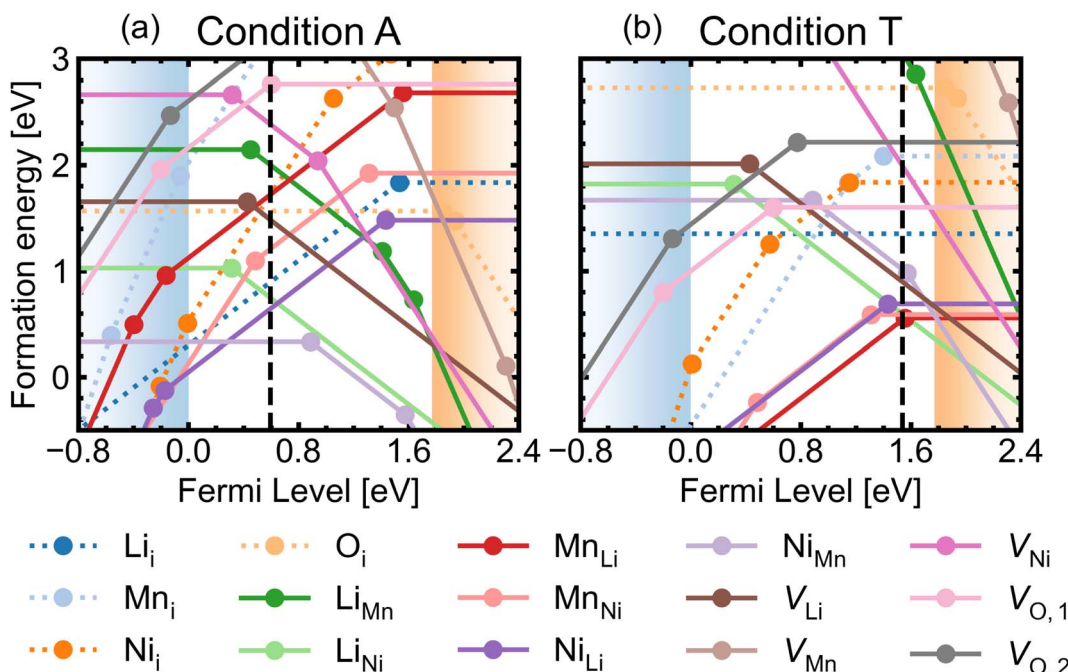


Fig. 5 Formation energies as a function of Fermi level for intrinsic defects in  $P4_332$   $LiMn_{1.5}Ni_{0.5}O_4$  under (a) O-rich (the most intrinsically p-type) condition A and (b) O-poor (the most intrinsically n-type) condition T. The self-consistent Fermi levels are denoted by the black dashed lines. Interstitial defects (dotted lines) and antisite and vacancy defects (solid lines) with the lowest energy charge states are shown, for clarity.

Below we discuss the lowest-formation-energy (highest concentration) defects at the self-consistent Fermi level, and their likely influences on material properties.

**Vacancies and antisites.** From Fig. 5, it is clear that among defects with  $E^f < 1$  eV, antisite defects dominate over other types of defects such as vacancies and interstitials. Under condition A, the formation energy of  $Ni_{Mn}^0$  is the lowest, at 0.33 eV. Followed by that are  $Ni_{Li}^+$  (0.64 eV) and  $Li_{Ni}^-$  (0.75 eV). Under condition T,  $Mn_{Li}^+$ ,  $Mn_{Ni}^0$ ,  $Li_{Ni}^-$  and  $Ni_{Li}^0$  have similar formation energies (0.5–0.7 eV). In both conditions, Fermi levels are pinned by compensating cation antisites in the band gap of this material.

Antisite behaviour is found to depend on the change in local coordination environment for the TM involved (e.g.  $O_h \rightarrow O_h$ ,  $O_h \rightarrow T_d$ ). For  $Mn_{Ni}$  and  $Ni_{Mn}$  with no change in coordination ( $O_h \rightarrow O_h$ ) at the defect site, fully ionised charge states (+2 and -2 respectively) give  $Mn^{4+}$  and  $Ni^{2+}$  species (see Table 3), while other charge states correspond to the addition of localised electrons/holes to the d orbitals of Mn/Ni, as confirmed by Bader charge density and the site-projected magnetisation analysis.<sup>100,101</sup> For example, the magnetisation on the  $Ni_{Mn}^0$  defect site is  $0.1 \mu_B$ , suggesting no unpaired electrons and corresponds to  $Ni^{4+}$  ( $d^6$ ) low-spin configuration. The local geometry near  $Ni^{4+}$  is slightly distorted with  $Ni^{4+}$ –O ranging between 1.85–1.88 Å which is shorter than that of  $Ni^{2+}$ –O = 2.06 Å (see Table 1). Similarly, the  $Mn_{Ni}^0$  defect site corresponds to  $Mn^{2+}$  ( $d^5$ ) high-spin of  $-4.5 \mu_B$ . The sign change in the magnetisation reflects a spin flip relative to Mn in the bulk and this is related to the complex orbital interactions exchanging the spin information.

Moorhead-Rosenberg *et al.*<sup>102</sup> suggested the spin on  $Mn^{3+}$  and  $Mn^{2+}$  should be parallel to that of  $Ni^{2+}$  due to the oxygen-mediated super-exchange interaction. This coincides with the spin-flip phenomena shown in Table 3. However, a spin flip is not observed on all defects and there is no clear trend whether a certain spin orientation is preferred. Magnetic interactions are influenced by the point defects and each defect has a complex potential energy surface, meaning that different defect structures and magnetic states may be found, depending on the initial structures, their magnetisation values and the choice of electronic minimisation algorithm. In each case, different degrees of structural perturbation (rattling) and magnetisation initialisations were tested, to aid the location of the true ground state defect.<sup>53–55</sup> One spin flip usually gives less than 0.1 eV difference in energy. However, multiple spin flips can lead to a large energy change (e.g.  $\sim 1$  eV) and give erroneous results. All calculations have been checked and rerun to ensure there are no multiple spin flips on the TM cations.

For  $Mn_{Li}$  and  $Ni_{Li}$  defects with a change in coordination ( $O_h \rightarrow T_d$ ) at the defect site, we observe a strong preference of Mn and Ni species to adopt the lowest stable positive oxidation states (a closer charge to  $Li^+$ ) for these elements (*i.e.*  $Mn^{2+}$  and  $Ni^{2+}$ ) (see Table 3). Ni coordinating to O in a  $T_d$  crystal field would favour a high-spin configuration as the size of ligand field splitting is reduced ( $\Delta_{T_d} = 4/9\Delta_{O_h}$ ), where  $\Delta_{T_d}$  and  $\Delta_{O_h}$  are the  $T_d$  and  $O_h$  crystal field splitting energy respectively.<sup>103</sup> The average bond lengths of  $T_d$   $Mn^{2+}$ –O is 1.98 Å, which is longer than the standard  $O_h$   $Mn^{4+}$ –O bond lengths between 1.87–1.94 Å (see Table 1). The energetic penalties for Ni to adopt  $Ni^{4+}$  ( $d^6$ ),  $Ni^{3+}$  ( $d^7$ ) and  $Ni^{2+}$  ( $d^8$ ) in a  $T_d$  field are  $2.13 \Delta_{O_h}$ ,  $1.26 \Delta_{O_h}$  and  $0.84$



**Table 3** Antisite defects ( $Mn_{Ni}$ ,  $Ni_{Mn}$ ,  $Mn_{Li}$  and  $Ni_{Li}$ ) in different charge states, site projected magnetisation, Bader charge and the species identities at defect sites

Defect	Magnetisation [ $\mu_B$ ]	Bader charge <sup>a</sup>	Species	Average TM–O bond lengths <sup>b</sup> [Å]
$Mn_{Ni}^{2+}$	3.1	1.84	$Mn^{4+}$ ( $d^3$ )	1.92
$Mn_{Ni}^+$	-3.7	1.70	$Mn^{3+}$ ( $d^4$ )	2.02
$Mn_{Ni}^0$	-4.5	1.46	$Mn^{2+}$ ( $d^5$ )	2.13
$Ni_{Mn}^{2-}$	1.7	1.22	$Ni^{2+}$ ( $d^8$ )	2.04
$Ni_{Mn}^-$	-0.9	1.32	$Ni^{3+}$ ( $d^7$ )	1.95
$Ni_{Mn}^0$	0.1	1.39	$Ni^{4+}$ ( $d^6$ )	1.87
$Mn_{Li}^{3+}$	4.4	1.50	$Mn^{2+}$ ( $d^5$ )	1.99
$Mn_{Li}^{2+}$	4.4	1.52	$Mn^{2+}$ ( $d^5$ )	1.98
$Mn_{Li}^+$	4.4	1.51	$Mn^{2+}$ ( $d^5$ )	1.98
$Mn_{Li}^0$	4.4	1.51	$Mn^{2+}$ ( $d^5$ )	1.98
$Ni_{Li}^{3+}$	-1.8	1.30	$Ni^{2+}$ ( $d^8$ )	1.94
$Ni_{Li}^{2+}$	-1.8	1.29	$Ni^{2+}$ ( $d^8$ )	1.94
$Ni_{Li}^+$	-1.8	1.29	$Ni^{2+}$ ( $d^8$ )	1.94
$Ni_{Li}^0$	-1.7	1.27	$Ni^{2+}$ ( $d^8$ )	1.93

<sup>a</sup> Bader charge in bulk LMNO (Wyckoff sites):  $Li^+$  (8c): 0.89;  $Mn^{4+}$  (12d): 1.81;  $Ni^{2+}$  (4b): 1.21;  $O_1^{2-}$  (24e): -1.06;  $O_2^{2-}$  (8c): -1.05. <sup>b</sup> Average TM–O bond length in bulk LMNO:  $Mn^{4+}$ –O: 1.91 Å;  $Ni^{2+}$ –O: 2.05 Å.

$\Delta_{O_h}$ , respectively, while for Mn in  $Mn^{4+}$  ( $d^3$ ),  $Mn^{3+}$  ( $d^4$ ) and  $Mn^{2+}$  ( $d^5$ ), they are 0.84  $\Delta_{O_h}$ , 0.42  $\Delta_{O_h}$  and 0  $\Delta_{O_h}$  respectively. Configurations with the lowest energetic penalties (*i.e.*  $Ni^{2+}$  and  $Mn^{2+}$ ) are favoured on the  $Li^{+}$  site. In addition, the ionic radius of  $Mn^{2+}$  in a four-coordination environment is 0.66 Å, which is closer to that of  $Li^+$  (0.59 Å), compared to  $Mn^{4+}$  (0.39 Å).<sup>104</sup> Literature studies<sup>2,7,21,105</sup> suggest the formation of  $Mn^{2+}$  as a consequence of  $Mn^{3+}$  disproportionation reactions.  $Mn^{2+}$  are detrimental to performance as they easily dissolve in electrolytes leading to capacity fading.<sup>23</sup> Additionally, our results may also explain the fact that Mn only exist in the reduced  $Mn^{2+}$  states upon migration from the  $O_h$  to the  $T_d$  sites during the structural transition upon heating highly delithiated LMNO.<sup>106</sup>

$Li_{TM}$  defects involve changing the coordination of Li ( $T_d$  →  $O_h$ ). We found that fully ionised  $Li_{Ni}^-$  is always the most stable charge state across all synthesis conditions at their self-consistent Fermi levels. In addition, the formation energies of  $Li_{Ni}^-$  are lower than  $Li_{Mn}$ , indicating that  $Li^+$  would preferentially form on the Ni sites over the Mn sites. Similar observations were found on Li-doped LMNO, where  $Li^+$  sat in the 4b positions.<sup>21</sup> This inevitably replaces some  $Ni^{2+}$ , leading to reduced capacity.

Among vacancy defects,  $V_O$  and  $V_{Li}$  have much lower formation energies (thus exist in higher concentrations) than  $V_{Mn}$  and  $V_{Ni}$  under all conditions (see Fig. 4). Therefore, oxygen and lithium vacancies are discussed here. For lithium vacancies, while  $V_{Li}^-$  (removing a  $Li^+$  ion) generates little disturbance to the system,  $V_{Li}^0$  (removing a Li atom) reveals the delithiation mechanism.<sup>16,86</sup> A localised hole is observed on the Ni in proximity to the defect site, with a magnetisation of -0.9  $\mu_B$  which is nearly half of the original value (-1.7  $\mu_B$ ) for  $Ni^{2+}$ . This suggests that  $Ni^{2+}$  ( $d^8$ ) is oxidised to  $Ni^{3+}$  ( $d^7$ ) low-spin configuration, with the Bader charge of 1.33 compared to 1.21 for bulk  $Ni^{2+}$  in agreement with the reduction in Ni–O bond lengths from 2.05 Å to 1.86–2.05 Å. The Ni–O bonds become more covalent and exhibit a JT distortion associated with  $d^7$  low-spin. Madelung potential analysis on the unrelaxed  $V_{Li}^0$  structure confirmed that

the nearest Ni to the vacant lithium site is oxidised to  $Ni^{3+}$ .<sup>107</sup> The average Madelung site potential on Ni is -24.55 V, whereas the  $Ni^{3+}$  site has the most negative potential, with -27.38 V.

Oxygen vacancies are found to be non-negative *U* type (stable in the 0 and +1 charge states, likely aided by polaronic stabilisation of excess electrons), adopting the neutral state under most growth conditions.<sup>108</sup>  $V_{O,1}$  are lower in energy than  $V_{O,2}$  at each charge state (Fig. 5). This can be explained from their local coordination as mentioned previously, with  $V_{O,1}$  configuration having less unfavourable electrostatic repulsion between the cations than that of  $V_{O,2}$ , reflected in the average Madelung potentials of 26.31 V ( $O_1$ ) and 29.37 V ( $O_2$ ). In the neutral state ( $V_{O,1}^0$  and  $V_{O,2}^0$ ), there are two five-coordinated  $Mn^{3+}$  which acquire the electrons donated from  $V_O$ , with magnetisation values between 3.6–3.7  $\mu_B$  compared to ~3.0 for the remaining  $Mn^{4+}$  species.  $Mn^{3+}$  have Bader charges ~1.6 which are lower than that of  $Mn^{4+}$ , with 1.83. In the +1 charge state,  $V_{O,1}^+$  has a localised electron on one of the five-coordinated Mn, whereas  $V_{O,2}^+$  has the additional electron delocalised over three five-coordinated Mn, confirmed by hybrid DFT calculations in a 56-atom supercell.

Overall, antisites and vacancies in LMNO are deep defects, generating localised states (that are distant from VBM and CBM) with small polarons on Mn sites for electrons and Ni for holes. The materials is dominated by ionic compensation rather than electronic compensation. The dopability of LMNO can be assessed by the size of the doping energy window, determined by the lowest energy compensating acceptor/donor defect at the CBM/VBM for n/p-type dopability.<sup>109</sup> The lowest energy donor and acceptor is antisite  $Ni_{Li}^+$  and  $Li_{Ni}^-$ , giving a dopability window of 0.05 eV (for p-type, O-rich) and 0.36 eV (for n-type, O-poor). Thus LMNO is potentially n-type dopable and not p-type dopable. This behaviour is driven by the antisites defects in LMNO rather than oxygen vacancies in other n-type oxides.<sup>110,111</sup>

**Interstitials.** In  $P4_332$  LMNO, there are two distinct types of vacant  $O_h$  sites: 4a and 12d sites which are surrounded by 3 $Mn^{4+}$



and  $3\text{Ni}^{2+}$  and  $5\text{Mn}^{4+}$  and a  $\text{Ni}^{2+}$ , respectively.<sup>112</sup> The lowest energy relaxed configurations of  $\text{Li}_i$  and  $\text{Ni}_i$  interstitials are in the 12d sites, whereas that of  $\text{Mn}_i$  are in the 4a sites. While the electrostatic interactions form a key contributor to the observed interstitial site preference, we find charge localisation, coordination environment and (potential) dumbbell formation to also play a key role.

For  $\text{Li}_i$ , a configuration with a Li–Li dumbbell split between neighbouring 12d sites is around 0.07 eV lower than a lone  $\text{Li}_i^+$  on the 12d site (see Fig. S3†). The preference for Li–Li dumbbell configuration was reported for the parent spinel compound LMO.<sup>86</sup> The Madelung potentials for  $\text{Li}^+$  in the  $\text{T}_d$  8c crystal site are around  $-9.54$  V, whereas those in the interstitial 4a and 12d are  $-6.84$  V and  $-6.40$  V respectively. Neutral  $\text{Li}_i^0$  gives an electron polaron on a neighbouring Mn (giving  $\text{Mn}^{3+}$ ) beside the Li–Li dumbbell.

For  $\text{TM}_i$ , the charge compensation mechanism for non-fully-ionised states is the same as for other n-type defects where  $\text{Mn}^{4+}$  in the proximity to the defect site get reduced. Having tested a range of charge states, we found  $\text{Mn}^{3+}$  and  $\text{Mn}^{2+}$  but no  $\text{Mn}^{4+}$  species in  $\text{Mn}_i$  defect supercells, whereas all Ni species always exist as  $\text{Ni}^{2+}$  in  $\text{Ni}_i$  defect supercells. When  $q = 2$ , interstitial Mn and Ni exist in +2 oxidation states. Adding more electrons in the systems ( $q = 1, 0$ ) led to the formation of more  $\text{Mn}^{3+}$ . Interstitial  $\text{Ni}^{2+}$  prefers to be in the 12d sites, identical to the preference for  $\text{Li}_i$ . Interstitial  $\text{Mn}^{2+}$ , on the other hand, prefers to be in the 4a sites ( $\sim 0.05$ – $0.15$  eV lower in energy). This could be partly due to a size effect. The 4a sites have larger octahedral volume than the 12d sites (Table S8†).<sup>112,113</sup> The ionic radii for  $\text{Li}^+$ ,  $\text{Ni}^{2+}$  and  $\text{Mn}^{2+}$  in octahedral coordination are  $0.76$  Å,  $0.69$  Å and  $0.83$  Å, respectively.<sup>104,113</sup> Ions with smaller ionic radii (*i.e.*  $\text{Li}^+$  and  $\text{Ni}^{2+}$ ) would have a smaller volume mismatch with the smaller 12d octahedral volume, while bigger  $\text{Mn}^{2+}$  need sites with larger volume. Similar to the structural features observed in  $\text{Li}_i$ , Li–Ni and Mn–Li split-interstitial configurations are also seen for  $\text{Ni}_i$  and  $\text{Mn}_i$ . This configuration reduces cation–cation repulsion and lattice strain, facilitated by highly mobile  $\text{Li}^+$  which can easily migrate from  $\text{T}_d$  to  $\text{O}_h$  sites.<sup>114</sup> Finally, the exchange type reaction  $\text{Ni}_i \rightarrow \text{Li}_i + \text{Ni}_{\text{Li}}$  is found to spontaneously occur, again reflecting the high mobility of  $\text{Li}^+$ .<sup>83</sup>

All  $\text{O}_i$  relaxed into dumbbell configurations with O–O distance within  $1.4$  Å.<sup>115</sup> In addition, they are stable in the charge neutral state over all Fermi levels, with high-lying O–O anti-bonding states. They are also known as peroxide species ( $\text{O}_{\text{per}}$ ) and are seen in many more n-type oxides (*e.g.*  $\text{SnO}_2$  and  $\text{BaSnO}_3$ ).<sup>54,110,116</sup> We identified two distinct  $\text{O}_i$  peroxide configurations with different TM environments: surrounded by  $3\text{Mn}^{4+}$  and a  $\text{Ni}^{2+}$  (ground state) and surrounded by  $2\text{Mn}^{4+}$  and  $2\text{Ni}^{2+}$  ( $0.8$  eV higher in energy).

Among all interstitial defects,  $\text{Li}_i$  is always lower in energy than  $\text{Mn}_i$  and  $\text{Ni}_i$ , indicating that they are more likely to form in high concentration. The energetic ordering of  $\text{Ni}_i$  and  $\text{Mn}_i$  can vary depending on the chemical potential conditions. The formation energy of  $\text{O}_i$  can become lower than that of  $\text{Li}_i$  in O-rich synthesis conditions. Overall,  $\text{Li}_i$ ,  $\text{Mn}_i$  and  $\text{Ni}_i$  are deep donors and  $\text{O}_i$  are ultra-deep acceptors with only neutral states stable across the band gap (see Fig. 5).

## Defect complexes

Given the low formation energies and thus high concentrations of cation antisites, lithium and oxygen vacancies, we further investigate the association of point defects, including three stoichiometric (antisite-pairs), and eight non-stoichiometric (vacancy-related) complexes. Since the formation energy on the oxygen vacancy in 24e sites ( $\text{O}_1$ ) is always lower and  $\text{O}_1$  has higher multiplicity than  $\text{O}_2$  (in the 8c sites), we only conduct detailed analysis on the association of  $\text{V}_{\text{Li}}$  with  $\text{V}_{\text{O}_1}$ .

Fig. 6 shows defect complex association energies  $\Delta H$  calculated following eqn (6) over 20 chemical potential limits at their self-consistent Fermi levels.  $\Delta H$  for a given complex can vary with chemical potentials, even for stoichiometric complexes, due to the indirect effect on the charge-balanced Fermi level. A negative  $\Delta H$  indicates an exothermic enthalpy change upon defect association. The majority of complexes have negative  $\Delta H$ , and they feature point defects coulombically attracted to each other. The few complexes that feature defects of the same charge (*i.e.* both p-type defects) are coulombically opposed to each other, and hence have positive  $\Delta H$  (*e.g.*  $\text{Li}_{\text{Ni}} - \text{V}_{\text{Li}}$ ). Using  $\Delta H$  alone to evaluate complex formation, however, neglects a key factor – the temperature dependent entropic cost of defect association. The actual formation of a defect complex and its concentration are influenced by a range of factors, including temperature, concentrations of the constituent defects and  $\Delta H$ .<sup>50,83</sup> We considered the entropic effects in this study by approximating the entropic term using eqn (10), where lower defect concentrations and higher temperatures correspond to larger entropic costs for association into defect complexes. Correspondingly, Fig. 7 shows how  $\Delta G$  increases with temperature, suggesting complex formation is sensitive to kinetic

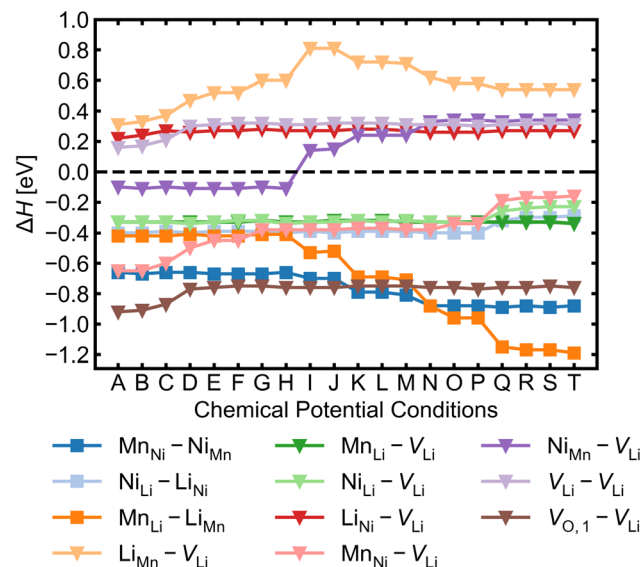


Fig. 6 Defect complex association energy  $\Delta H$  for a selection of stoichiometric complexes (denoted by squares) and non-stoichiometric complexes (denoted by triangles) calculated at the self-consistent Fermi level over 20 different growth conditions from A (O-rich, p-type) to T (O-poor, n-type).



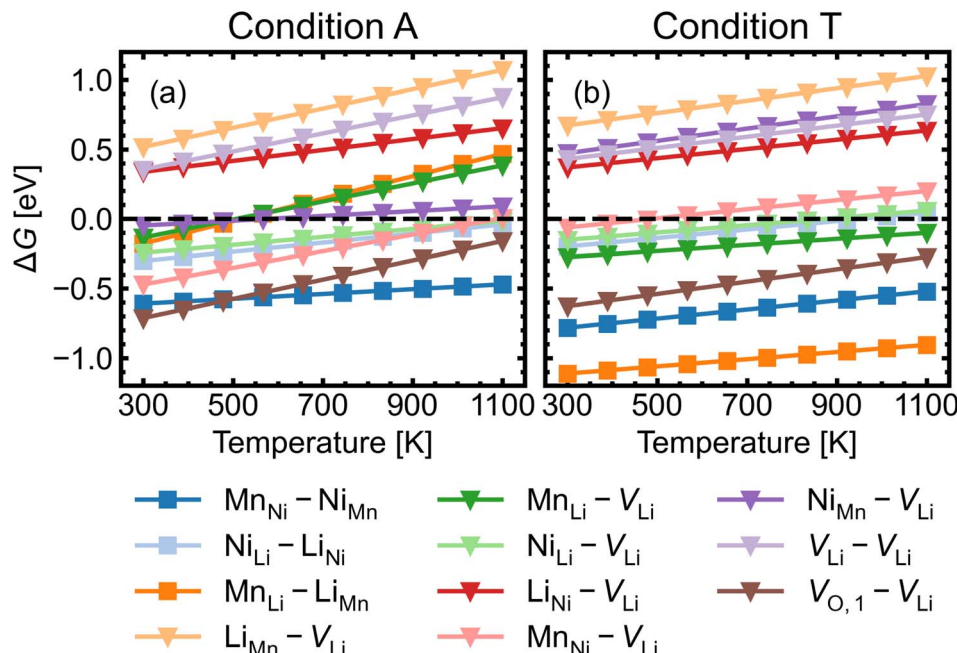


Fig. 7 Gibbs free energy change  $\Delta G$  for complex formation as a function of temperature under (a) the most intrinsically p-type O-rich condition A and (b) n-type O-poor condition T, using eqn (10). Stoichiometric complexes are denoted by squares and non-stoichiometric complexes are denoted by triangles. A negative  $\Delta G$  suggests complex association is likely, provided the constituent point defects are sufficiently mobile.

behaviour during synthesis and quenching.  $\Delta G$  are generally more negative in the n-type condition than p-type, suggesting that there is a stronger driving force towards complex association even at high temperature in O-poor conditions.

Fig. 8 shows the approximated temperature-dependent entropic cost (calculated using eqn (10)) for defect complexes

with negative  $\Delta G$ . A high degree of association is achieved when the complex association energy magnitude  $|\Delta H|$  is greater than  $\Delta E_{\text{crit}}$ , showing that one cannot use  $\Delta H$  alone to evaluate complex formation. For example, under the intrinsically p-type environment (Fig. 8a), the  $\text{Mn}_{\text{Li}}\text{-Li}_{\text{Mn}}$  association energy  $|\Delta H| = 0.4$  eV is only sufficient to achieve a high degree of association at

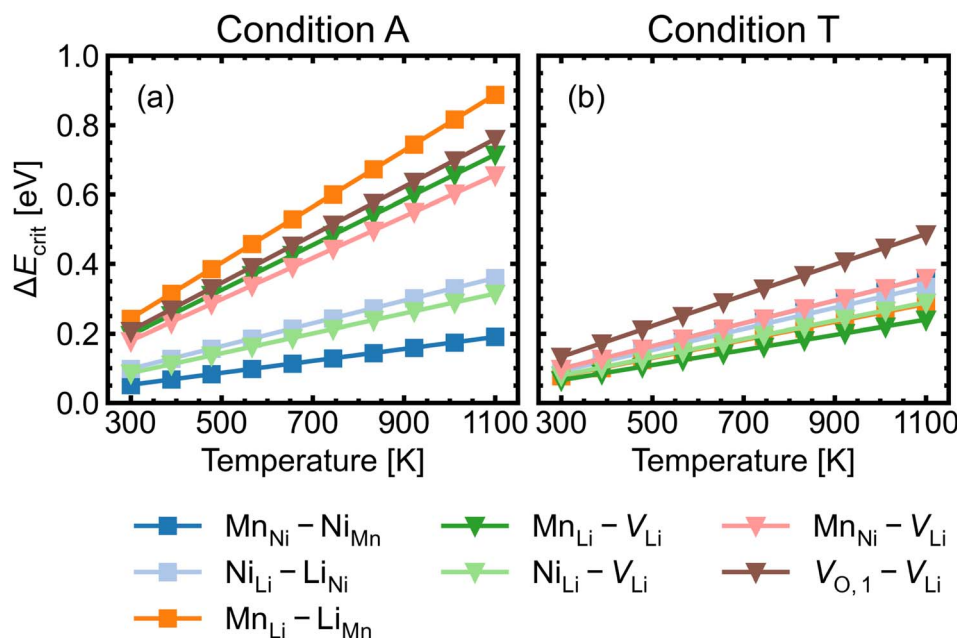


Fig. 8 Critical association energy  $\Delta E_{\text{crit}}$  (approximate entropic cost of complex formation; eqn (10)) as a function of temperature under (a) the most intrinsically p-type O-rich condition A and (b) n-type O-poor condition T. Stoichiometric complexes are denoted by squares and non-stoichiometric complexes are denoted by triangles.



500 K but not at 900 K. Increased entropic cost of complex formation is observed for defects with lower concentration (see Fig. 9). The stoichiometric complexes have identical density of the available microstates ( $N_{\text{states}} = 4.40 \times 10^{22} \text{ cm}^{-3}$ ), the differences in the calculated complex concentrations therefore arise from the concentrations of their constituent point defects. For instance, under condition T (Fig. 9b),  $[\text{Mn}_{\text{Li}}\text{--Li}_{\text{Mn}}]$  is lower than  $[\text{Ni}_{\text{Li}}\text{--Li}_{\text{Ni}}]$  at the majority of temperature range despite that they have similar  $\Delta E_{\text{crit}}$  and that  $\Delta H$  for  $\text{Mn}_{\text{Li}}\text{--Li}_{\text{Mn}}$  is highly negative (see Fig. 6). Although complex formation is more favourable at lower temperature, this requires isolated point defects to "find" each other. Point defects with high mobility – such as lithium vacancies and interstitials – and/or those that with high concentration are likely to achieve this criterion.

$\text{Mn}_{\text{Ni}}\text{--Ni}_{\text{Mn}}$  has the highest concentration for maximum (>99%) complex formation (*i.e.* saturation concentration), reflecting the strong proclivity to  $\text{Mn}_{\text{Ni}}\text{--Ni}_{\text{Mn}}$  cation disorder in LMNO. Complexes (*e.g.*  $\text{Mn}_{\text{Li}}\text{--Li}_{\text{Mn}}$ ) with much lower predicted concentration contribute much less to the disorder. Since defect complex concentrations are higher in condition T than condition A, a greater range of disorder is induced by complex formation under O-poor conditions. In addition, there is a variable temperature-dependent entropic cost with complex formation, with higher defect concentrations corresponding to lower entropic costs of complex association. For example,  $V_{\text{O},1}\text{--V}_{\text{Li}}$  concentration is strongly dependent on temperature, whereas it is not the case for  $\text{Ni}_{\text{Li}}\text{--V}_{\text{Li}}$ . High synthesis/anneal temperatures will yield high point defect concentrations (eqn (7)), which then increasingly favour complex formation as the material cools to room temperature, but with the ability to equilibrate by migrating and forming complexes also

decreasing with temperature. Thus the final defect distribution in the material is predicted to be sensitively dependent on the thermal history (*i.e.* synthesis, annealing and cooling procedures), as witnessed experimentally.<sup>117</sup>

The association of lithium vacancies with other defects can affect lithium diffusion. If  $V_{\text{Li}}$  preferentially associates with a specific point defect, the additional species may function as a "trap" for diffusing lithium. Previous literature studies<sup>29,118</sup> have specifically discussed the  $V_{\text{O},1}\text{--V}_{\text{Li}}$  complex, with  $\text{Li}^+$  diffusion more difficult in disordered LMNO, as lithium vacancies preferentially form near oxygen vacancies – which have formation energies  $\sim 1$  eV lower in the disordered material. Our calculations indeed find strongly favourable complex binding energies for  $V_{\text{O},1}\text{--V}_{\text{Li}}$ , as well as the moderate binding for  $\text{Mn}_{\text{Li}}\text{--V}_{\text{Li}}$  and  $\text{Mn}_{\text{Ni}}\text{--V}_{\text{Li}}$  (Fig. 7). Thus O-rich conditions (*e.g.* Condition A) are expected to minimise the number of lithium traps ( $X\text{--V}_{\text{Li}}$  complexes), but also yield decreased lithium vacancy concentrations, exhibiting opposing effects on the overall diffusion rate. Therefore,  $\text{Li}^+$  mobility is affected by competing interactions between other point defects with strong attraction to lithium vacancies, and is highly sensitive to the synthesis environment.

### Defect migration

Diffusion of  $\text{Li}^+$  is a fundamental process that occurs during charge/discharge of a cathode. In a spinel framework like LMNO,  $\text{Li}^+$  migration occurs from a  $T_d$  site to another  $T_d$  site *via* an empty  $O_h$  (gate) site. There are two different gate sites (4a and 12d) in  $P4_332$  LMNO and thus two distinct migration paths for  $\text{Li}^+$  (see Fig. 10). Li diffusivity calculations have been used to explain the rate capabilities of LMNO. Most theoretical

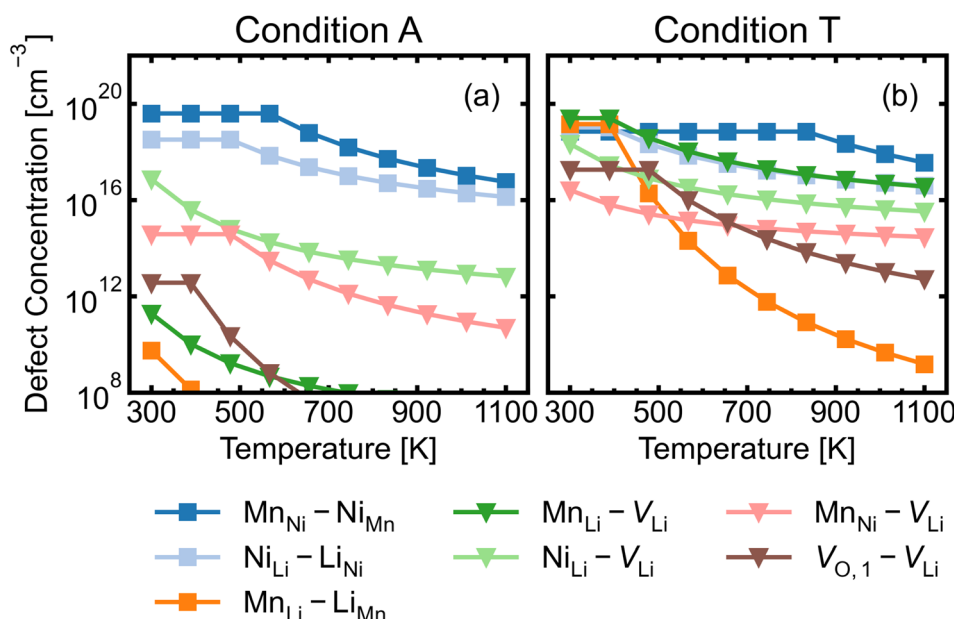


Fig. 9 Defect complex concentration as a function of temperature under (a) the most intrinsically p-type O-rich condition A and (b) n-type O-poor condition T, using eqn (7). Constituent point defect concentrations are fixed to the calculated concentrations at the anneal temperature ( $T = 973$  K), following the typical frozen-defect approximation. Stoichiometric complexes are denoted by squares and non-stoichiometric complexes are denoted by triangles. Defect complex concentrations are capped at the concentration of the major constituent defect.



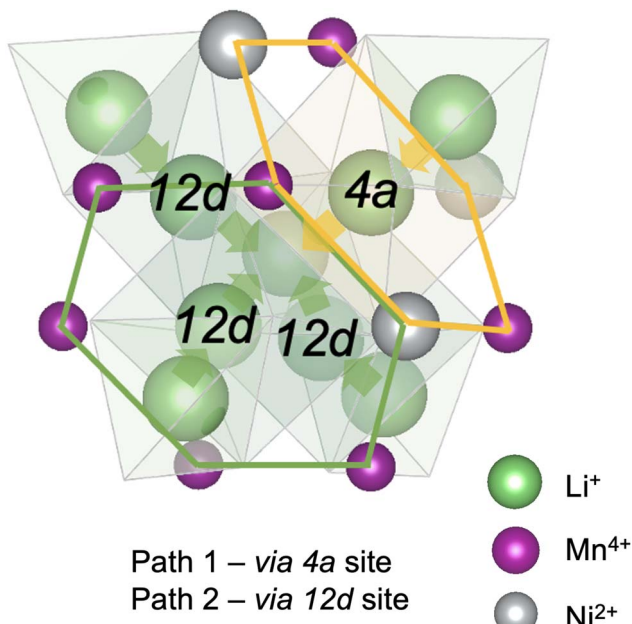


Fig. 10 A schematic showing 4a and 12d gate sites giving two distinct  $\text{Li}^+$  migration paths in  $\text{P4}_3\text{32 LiMn}_{1.5}\text{Ni}_{0.5}\text{O}_4$ . The 4a site surrounded by  $3\text{Mn}^{4+}$  and  $3\text{Ni}^{2+}$ ; the 12d sites surrounded by  $5\text{Mn}^{4+}$  and a  $\text{Ni}^{2+}$ . Path 1 and path 2 are denoted by yellow and green arrows, respectively. Oxygen atoms which define the polyhedral vertices are not shown for clarity.

studies<sup>112,118,119</sup> have considered the diffusion of  $\text{Li}^+$  *via* the vacancy mechanism, which involves hopping of a single  $\text{Li}^+$  from one site to another ( $V_{\text{Li}}$  hopping in the opposite direction). Our calculated  $\text{Li}^+$  migration barriers *via* the vacancy mechanism (Fig. 11) are similar to previous studies.<sup>118,119</sup> The

activation energies for  $\text{Li}^+$  to migrate through 4a (path 1) and 12d (path 2) gate sites are 0.34 eV and 0.30 eV, respectively. This is consistent with our findings that Li interstitials preferentially sit on the 12d sites.

We also considered  $\text{Li}^+$  migration *via* an interstitialcy mechanism, which has not been previously studied in LMNO. This involves concerted migration of three  $\text{Li}^+$ : two ions of the Li-Li dumbbell and one ion that is next to the dumbbell. The path 1 end image is higher in energy, where one of the  $\text{Li}^+$  in the Li-Li dumbbell sits on a 4a site. The path 2 end image is an equivalent configuration to the initial image where both  $\text{Li}^+$  in Li-Li dumbbell sit on 12d sites. The activation energies to migrate through path 1 and path 2 are 0.14 eV and 0.12 eV, respectively. Again, migrating *via* 4a sites is less favourable. Nevertheless, the activation energies for  $\text{Li}^+$  to migrate *via* the interstitialcy mechanism are much lower than that *via* the vacancy mechanism. This suggests that the dominant diffusion mechanism may change during charge and discharge. Since the interstitialcy mechanism involves concerted migration of multiple  $\text{Li}^+$  *via* the Li-Li dumbbell configuration, this migration is only possible when the concentration of  $\text{Li}^+$  is sufficiently high and it has also been shown that migration barriers can vary with Li concentration due to effects on Ni valence and thus electrostatic interactions between Li.<sup>112,120</sup>

Finally, we show that the  $\text{Li}^+$  interstitialcy migration makes the Li-Frenkel pair ( $\text{Li}^+ - V_{\text{Li}}$ ) unstable to spontaneous recombination at short pair distances. To investigate this, a Li vacancy was placed with a Li interstitial over each of the six standard positions over a range of pair distances for each calculation. From the cNEB calculations, we determine a critical spontaneous recombination distance of  $\sim 4.6 \text{ \AA}$ , which is larger than the minimum separation ( $3.45 \text{ \AA}$ ) between Li in their  $\text{T}_d$  sites.

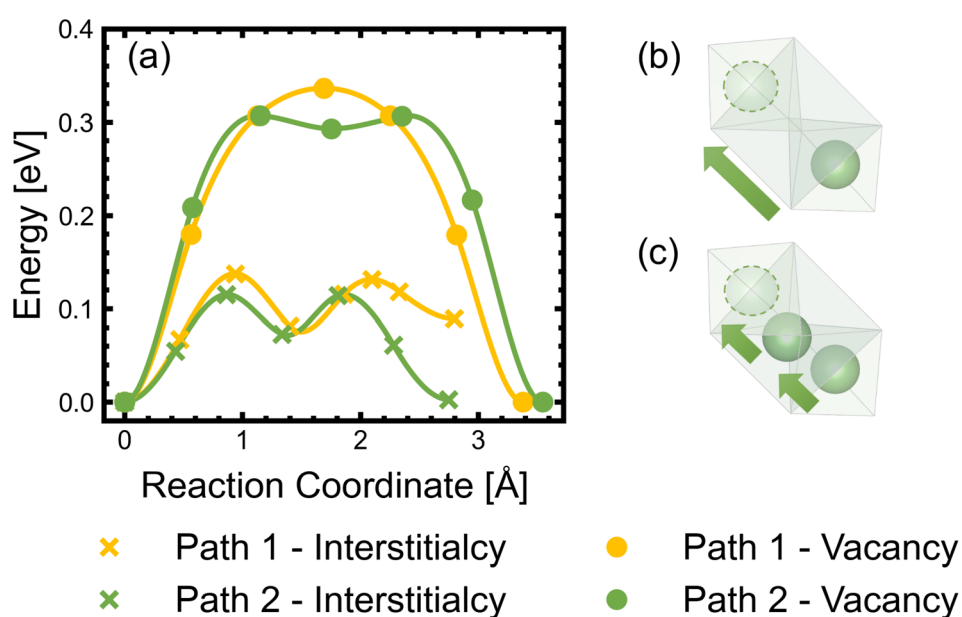


Fig. 11 (a) Migration barriers of lithium interstitials ( $\text{Li}^+$ ) *via* interstitialcy mechanisms and lithium vacancies ( $V_{\text{Li}}$ ) *via* vacancy mechanisms, calculated using the climbing-image nudged elastic band (cNEB) method. Path 1 and path 2 involve  $\text{Li}^+$  migrating through the 4a sites (surrounded by  $3\text{Mn}^{4+}$  and  $3\text{Ni}^{2+}$ ) and 12d sites (surrounded by  $5\text{Mn}^{4+}$  and a  $\text{Ni}^{2+}$ ), respectively. Schematic illustrations of the (single-ion) vacancy migration (b) and (concerted multi-ion) interstitialcy migration (c).



### Self-consistent Fermi levels

While most discussions around defect chemistry are focused on two distinct O-rich (p-type)/O-poor (n-type) growth conditions, we would like to highlight that defect chemistry can be different in other intermediate growth conditions. Fig. 12 shows the calculated self-consistent Fermi level in all growth conditions. Since the ideal synthesis/anneal temperature for the ordered phase is at 700 °C, 973 K is used as the input temperature to determine the self-consistent Fermi levels.<sup>1,12,20,21</sup> The chemical potential conditions A → T are arranged with increasing self-consistent Fermi level. To understand the defect behaviour at room/operating temperature, self-consistent Fermi levels were also calculated with constant non-lithium defect concentrations upon cooling (*i.e.* “frozen in”). While the kinetic barriers of non-lithium defects can be assumed to be large, the same assumption can not be applied to lithium defects ( $V_{Li}$  and  $Li_{Li}$ ) as the facile movement of  $Li^+$  is one of the desirable features for a cathode.<sup>121</sup> In addition, it has been suggested that some lithium vacancy-interstitial pairs would recombine (*i.e.* the reverse reaction of Frenkel pair formation) at lower temperatures.<sup>122,123</sup> Two variations of the “frozen” approach were applied. The former approach only allowed  $V_{Li}$  and  $Li_{Li}$  concentrations to vary, whereas the latter also allowed  $Li_{Mn}$  and  $Li_{Ni}$  concentrations to change.

The majority of conditions have Fermi levels  $\pm 0.5$  eV from the mid gap. Under the most O-poor conditions, the Fermi level is  $\leq 0.24$  eV away from the CBM. Therefore, the material is a weak semiconductor, and can be made more n-type than p-type. The intrinsic defects are not likely to generate significant quantities of free charge carriers that contribute to conductivity and electronic conduction would be mainly governed by the hopping of small polarons.<sup>86</sup> This type of transport behaviour gives weaker electronic conduction compared to those *via* band-

like carriers and shows a strong sensitivity to temperature due to their thermally activated hopping processes.  $Ni^{3+}/Mn^{3+}$  are the dominant charge compensating ions under all conditions. In addition,  $Mn^{2+}$  formation is frequently observed for n-type defects, suggesting a strong driving force for  $Mn^{3+}$  to undergo disproportionation reactions.

The formation of oxygen vacancies and  $Mn^{3+}$  is a dominant feature when LMNO is synthesized at a more O-poor (n-type) condition. The electrochemical performance of LMNO synthesized under those conditions can be improved due to the increase in cation disorder and the proportion of  $Mn^{3+}$ .<sup>12</sup> While  $Mn^{3+}$  species is redox active which improves the electronic conductivity, it is subject to JT distortion and promotes Mn dissolution. Therefore,  $[Mn^{3+}]$  should be controlled to achieve optimum performance. Ni-rich rock salt impurity phases are also likely to form under n-type conditions. This is not desirable as it leads to a decrease in capacity. Fig. S5† shows that oxygen vacancies remain at a low concentration ( $\ll 1\%$ ) in different growth environments when the spinel remains in the  $P4_{3}32$  arrangement. Therefore, the cation ordered LMNO is not prone to be oxygen deficient and this is in line with previous studies.<sup>28,29,99</sup> Despite the low concentration of oxygen vacancies, the fact that they exist over a range of magnitudes suggests that they can be controlled independently with regards to the cation ordering. In fact, they are highly dependent on the oxygen environment and Fermi level.

Since antisite defects are generally low energy over all chemical potential conditions, we propose that (local) cation ordering can be perturbed under many different synthesis conditions. This supports previous experimental studies<sup>13,20,21</sup> where local Mn/Ni ordering has been perturbed without significant concentrations of oxygen vacancies and/or  $Mn^{3+}$ . Theoretically, O-rich (p-type) conditions have a higher tendency towards  $Ni^{3+}$  formation. For samples which undergo a series of heat treatment processes, a more p-type condition could oxidise the pre-formed  $Mn^{3+}$  back to  $Mn^{4+}$ , reducing the total number of redox active centers and leading to reduced capacity. Synthesis techniques that can take the advantage of the inherent defect chemistry of the material are more likely to achieve the fine tuning of electrochemical performance with target features. For example, Lee *et al.*<sup>21</sup> utilised the preference for  $Li_{Ni}$  antisite formation (on the 4b sites) to block the Mn/Ni ordering transition pathways during the annealing process of the Li-doped LMNO samples. Their Li-doped LMNO “ $Mn^{3+}$ -free” samples annealed at 700 °C exhibited increased Mn/Ni disordering and showed enhanced cycling stability. In this case, the undesirable effects from  $Mn^{3+}$  had been suppressed, as the  $Mn^{3+}$  generated during the first (900 °C) treatment were re-oxidised to  $Mn^{4+}$  when annealed at 700 °C. Unfortunately, the high concentration of  $Li_{Ni}$  defects leads to a reduced capacity. The defect chemistry of LMNO therefore plays a crucial role in affecting the electrochemical performance. To design LMNO with optimum electrochemical performance, it is important to account for defect behaviour and effectively utilise it when developing synthesis methods.

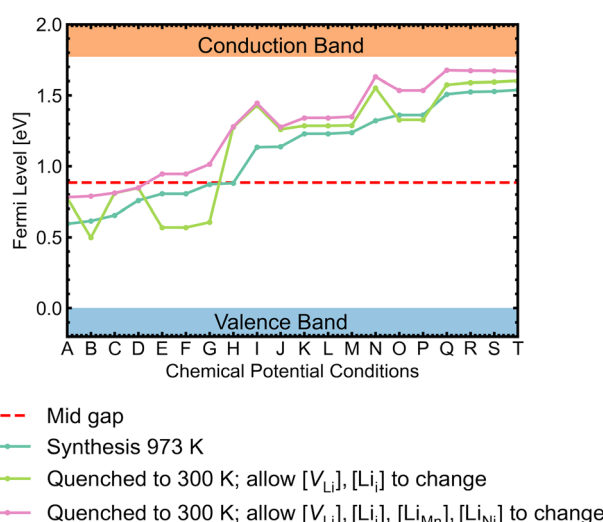


Fig. 12 Self-consistent Fermi levels determined under all chemical potential conditions. The atomic chemical potential values can be found in Table S6.† Two variant approaches assuming certain defects are “frozen in” during synthesis were adopted to simulate defect behaviours at room temperature (300 K).



## Conclusions

The bulk properties of  $P4_332$  LMNO and its intrinsic defect chemistry have been investigated using DFT. To correctly capture the magnetic properties and ground state electronic structure, we demonstrated the importance of a systematic evaluation of the magnetic ordering in the open-shell TM system. Analysis of the electronic structures indicated a high degree of hybridisation of Ni–O and Mn–O states in LMNO. The thermodynamic stability of LMNO is more sensitive to Ni chemical potentials, while there is a greater flexibility to vary the Li and Mn chemical potentials, leading to different defect properties.

The intrinsic defect chemistry suggests LMNO a weak semiconductor and can be made more n-type. The formation of deep defects and small polarons indicated electronic conduction proceeds *via* the polaron hopping mechanism. The low formation energies for antisite defects explain the tendency towards cation disordering. There exist several defect pair complexes with strong association energies and they are sensitive to the experimental conditions and thermal history of the material. The investigation of Li defects migration revealed that  $Li^+$  can migrate *via* a much lower energy concerted multi-ion interstitialcy mechanism than the previously proposed vacancy mechanism. However, this is achieved *via* low energy Li–Li dumbbell configuration and requires sufficiently mobile  $Li^+$ . The  $Li^+$  mobility is influenced by the interactions with point defects.

A comprehensive analysis of the defect chemistry over all growth conditions shows a tendency toward O-poor (n-type) conditions where  $Mn^{3+}$  formation is encouraged. This may explain why many experimental studies find it challenging to study solely the effect of Mn/Ni ordering on the electrochemical performance. Despite the material being a weak semiconductor, the strong dependency of defect concentrations on the Fermi level indicates that out-of-equilibrium synthesis methods and aliovalent doping can, to certain extent, change the defect landscape to fine tune the level of Ni-deficiency and  $Mn^{3+}$  content. Our work demonstrates that a deep understanding of the defect chemistry can help to establish connections between conflicting experimental findings. This work also provides a basis for understanding the charge compensation mechanisms of extrinsic defects. Finally, the success of a complete defect survey on LMNO suggests that this approach can be extended to understand the chemistries of other complex battery materials.

## Conflicts of interest

There are no conflicts to declare.

## Acknowledgements

This work was supported by the Faraday Institution grant number FIRG017 and used the Michael supercomputer (FIRG030). S. R. K. acknowledges the EPSRC Centre for Doctoral Training in the Advanced Characterisation of Materials (CDT-

ACM) (EP/S023259/1) for funding a PhD studentship. *Via* our membership of the UK's HEC Materials Chemistry Consortium, which is funded by the UK Engineering and Physical Sciences Research Council (EPSRC; EP/L000202, EP/R029431, EP/T022213), this work used ARCHER2 UK National Supercomputing Services. We are also grateful to the UK Materials and Molecular Modelling Hub (MMM Hub), which is partially funded by the EPSRC (EP/P020194/1, EP/T022213/1), for computational resources on the Thomas, Young supercomputers, and to UCL for access to the Myriad (Myriad@UCL) and Kathleen (Kathleen@UCL) supercomputers.

## References

- 1 G. Liang, V. K. Peterson, K. W. See, Z. Guo and W. K. Pang, Developing High-Voltage Spinel  $LiNi_{0.5}Mn_{1.5}O_4$  Cathodes for High-Energy-Density Lithium-Ion Batteries: Current Achievements and Future Prospects, *J. Mater. Chem. A*, 2020, **8**, 15373–15398.
- 2 Y. Huang, Y. Dong, S. Li, J. Lee, C. Wang, Z. Zhu, W. Xue, Y. Li and J. Li, Lithium Manganese Spinel Cathodes for Lithium-Ion Batteries, *Adv. Energy Mater.*, 2020, 2000997.
- 3 M. M. Thackeray and K. Amine,  $LiMn_2O_4$  Spinel and Substituted Cathodes, *Nat. Energy*, 2021, **6**, 566.
- 4 Q. Zhong, A. Bonakdarpour, M. Zhang, Y. Gao and J. R. Dahn, Synthesis and Electrochemistry of  $LiNi_xMn_{2-x}O_4$ , *J. Electrochem. Soc.*, 1997, **144**, 205–213.
- 5 W. Xiao, C. Xin, S. Li, J. Jie, Y. Gu, J. Zheng and F. Pan, Insight into Fast Li Diffusion in Li-excess Spinel Lithium Manganese Oxide, *J. Mater. Chem. A*, 2018, **6**, 9893–9898.
- 6 Z. Wan, Y. Xu, G. Sun, D. Xu and X. Luo, Conflicting Role of Inversion of the  $LiMn_2O_4$  Spinel on Lithium-Ion Battery Capacity from First-Principles Calculations, *J. Phys. Chem. C*, 2022, **126**, 7374–7382.
- 7 G. Zhou, X. Sun, Q.-H. Li, X. Wang, J.-N. Zhang, W. Yang, X. Yu, R. Xiao and H. Li, Mn Ion Dissolution Mechanism for Lithium-Ion Battery with  $LiMn_2O_4$  Cathode: In Situ Ultraviolet-Visible Spectroscopy and Ab Initio Molecular Dynamics Simulations, *J. Phys. Chem. Lett.*, 2020, **11**, 3051–3057.
- 8 T. Liu, *et al.*, Correlation between Manganese Dissolution and Dynamic Phase Stability in Spinel-Based Lithium-Ion Battery, *Nat. Commun.*, 2019, **10**, 4721.
- 9 J.-H. Kim, S.-T. Myung, C. S. Yoon, S. G. Kang and Y.-K. Sun, Comparative Study of  $LiNi_{0.5}Mn_{1.5}O_{4-\delta}$  and  $LiNi_{0.5}Mn_{1.5}O_4$  Cathodes Having Two Crystallographic Structures:  $Fd\bar{3}m$  and  $P4_332$ , *Chem. Mater.*, 2004, **16**, 906–914.
- 10 G. Liu, J. Zhang, X. Zhang, Y. Du, K. Zhang, G. Li, H. Yu, C. Li, Z. Li, Q. Sun and L. Wen, Study on Oxygen Deficiency in Spinel  $LiNi_{0.5}Mn_{1.5}O_4$  and Its Fe and Cr-doped Compounds, *J. Alloys Compd.*, 2017, **725**, 580–586.
- 11 M. Kunduraci and G. G. Amatucci, Synthesis and Characterization of Nanostructured 4.7 V  $Li_xMn_{1.5}Ni_{0.5}O_4$  Spinels for High-Power Lithium-Ion Batteries, *J. Electrochem. Soc.*, 2006, **153**, A1345.
- 12 K. Lee, G. J. Yang and Y. Kim, Improvement of the Electrochemical Properties of  $LiNi_{0.5}Mn_{1.5}O_4$  by



Controlling the Heating Atmosphere during Synthesis, *Ceram. Int.*, 2017, **43**, 15510–15518.

13 B. Aktekin, M. Valvo, R. I. Smith, M. H. Sørby, F. Lodi Marzano, W. Zipprich, D. Brandell, K. Edström and W. R. Brant, Cation Ordering and Oxygen Release in  $\text{LiNi}_{0.5-x}\text{Mn}_{1.5+x}\text{O}_{4-y}$  (LNMO): In Situ Neutron Diffraction and Performance in Li Ion Full Cells, *ACS Appl. Energy Mater.*, 2019, **2**, 3323–3335.

14 H. Duncan, B. Hai, M. Leskes, C. P. Grey and G. Chen, Relationships between  $\text{Mn}^{3+}$  Content, Structural Ordering, Phase Transformation, and Kinetic Properties in  $\text{LiNi}_x\text{Mn}_{2-x}\text{O}_4$  Cathode Materials, *Chem. Mater.*, 2014, **26**, 5374–5382.

15 J. Yoon, D. Kim, J. H. Um, M. Jeong, W. Oh and W.-S. Yoon, Effect of Local Structural Changes on Rate Capability of  $\text{LiNi}_{0.5}\text{Mn}_{1.5}\text{O}_{4-\delta}$  Cathode Material for Lithium Ion Batteries, *J. Alloys Compd.*, 2016, **686**, 593–600.

16 F. A. Vásquez, N. C. Rosero-Navarro, A. Miura, R. Jalem, Y. Goto, M. Nagao, Y. Tateyama, K. Tadanaga and J. A. Calderón, Kinetic Control of the  $\text{Li}_{0.9}\text{Mn}_{1.6}\text{Ni}_{0.4}\text{O}_4$  Spinel Structure with Enhanced Electrochemical Performance, *ACS Appl. Mater. Interfaces*, 2021, **13**, 14056–14067.

17 H. Ryoo, H. B. Bae, Y.-M. Kim, J.-G. Kim, S. Lee and S.-Y. Chung, Frenkel-Defect-Mediated Chemical Ordering Transition in a Li-Mn-Ni Spinel Oxide, *Angew. Chem.*, 2015, **54**, 7963–7967.

18 D. Liu, W. Zhu, J. Trottier, C. Gagnon, F. Baray, A. Guerfi, A. Mauger, H. Groult, C. M. Julien, J. B. Goodenough and K. Zaghib, Spinel Materials for High-Voltage Cathodes in Li-ion Batteries, *RSC Adv.*, 2014, **4**, 154–167.

19 J. Liu, A. Huq, Z. Moorhead-Rosenberg, A. Manthiram and K. Page, Nanoscale Ni/Mn Ordering in the High Voltage Spinel Cathode  $\text{LiNi}_{0.5}\text{Mn}_{1.5}\text{O}_4$ , *Chem. Mater.*, 2016, **28**, 6817–6821.

20 M. Casas-Cabanas, C. Kim, J. Rodríguez-Carvajal and J. Cabana, Atomic Defects during Ordering Transitions in  $\text{LiNi}_{0.5}\text{Mn}_{1.5}\text{O}_4$  and Their Relationship with Electrochemical Properties, *J. Mater. Chem. A*, 2016, **4**, 8255–8262.

21 J. Lee, N. Dupre, M. Avdeev and B. Kang, Understanding the Cation Ordering Transition in High-Voltage Spinel  $\text{LiNi}_{0.5}\text{Mn}_{1.5}\text{O}_4$  by Doping Li Instead of Ni, *Sci. Rep.*, 2017, **7**, 6728.

22 J. Cabana, M. Casas-Cabanas, F. O. Omenya, N. A. Chernova, D. Zeng, M. S. Whittingham and C. P. Grey, Composition-Structure Relationships in the Li-Ion Battery Electrode Material  $\text{LiNi}_{0.5}\text{Mn}_{1.5}\text{O}_4$ , *Chem. Mater.*, 2012, **24**, 2952–2964.

23 A. B. Haruna, P. Mwonga, D. Barrett, C. B. Rodella, R. P. Forbes, A. Venter, Z. Sentsho, P. J. Fletcher, F. Marken and K. I. Ozoemena, Defect-Engineered  $\beta\text{-MnO}_{2-\delta}$  Precursors Control the Structure–Property Relationships in High-Voltage Spinel  $\text{LiMn}_{1.5}\text{Ni}_{0.5}\text{O}_{4-\delta}$ , *ACS Omega*, 2021, **6**, 25562–25573.

24 J. Xiao, X. Chen, P. V. Sushko, M. L. Sushko, L. Kovarik, J. Feng, Z. Deng, J. Zheng, G. L. Graff, Z. Nie, D. Choi, J. Liu, J.-G. Zhang and M. S. Whittingham, High-Performance  $\text{LiNi}_{0.5}\text{Mn}_{1.5}\text{O}_4$  Spinel Controlled by  $\text{Mn}^{3+}$  Concentration and Site Disorder, *Adv. Mater.*, 2012, **24**, 2109–2116.

25 D. W. Shin, C. A. Bridges, A. Huq, M. P. Paranthaman and A. Manthiram, Role of Cation Ordering and Surface Segregation in High-Voltage Spinel  $\text{LiMn}_{1.5}\text{Ni}_{0.5-x}\text{M}_x\text{O}_4$  ( $\text{M} = \text{Cr, Fe, and Ga}$ ) Cathodes for Lithium-Ion Batteries, *Chem. Mater.*, 2012, **24**, 3720–3731.

26 C. Freysoldt, B. Grabowski, T. Hickel, J. Neugebauer, G. Kresse, A. Janotti and C. G. Van de Walle, First-Principles Calculations for Point Defects in Solids, *Rev. Mod. Phys.*, 2014, **86**, 253–305.

27 D. O. Scanlon, J. Buckeridge, C. R. A. Catlow and G. W. Watson, Understanding Doping Anomalies in Degenerate P-Type Semiconductor  $\text{LaCuOSe}$ , *J. Mater. Chem. C*, 2014, **2**, 3429–3438.

28 H. Shiiba, N. Zettsu, M. Nakayama, S. Oishi and K. Teshima, Defect Formation Energy in Spinel  $\text{LiNi}_{0.5}\text{Mn}_{1.5}\text{O}_{4-\delta}$  Using Ab Initio DFT Calculations, *J. Phys. Chem. C*, 2015, **119**, 9117–9124.

29 P. V. Sushko, K. M. Rosso, J.-G. Zhang, J. Liu and M. L. Sushko, Oxygen Vacancies and Ordering of D-Levels Control Voltage Suppression in Oxide Cathodes: The Case of Spinel  $\text{LiNi}_{0.5}\text{Mn}_{1.5}\text{O}_{4-\delta}$ , *Adv. Funct. Mater.*, 2013, **23**, 5530–5535.

30 Y. Chen, Y. Sun and X. Huang, Origin of the Ni/Mn Ordering in High-Voltage Spinel  $\text{LiNi}_{0.5}\text{Mn}_{1.5}\text{O}_4$ : The Role of Oxygen Vacancies and Cation Doping, *Comput. Mater. Sci.*, 2016, **115**, 109–116.

31 S. Kim, S. N. Hood, J.-S. Park, L. D. Whalley and A. Walsh, Quick-Start Guide for First-Principles Modelling of Point Defects in Crystalline Materials, *J. Phys.: Energy*, 2020, **2**, 036001.

32 C. Freysoldt, J. Neugebauer and C. G. Van de Walle, Electrostatic Interactions between Charged Defects in Supercells, *Phys. Status Solidi B*, 2011, **248**, 1067–1076.

33 G. Kresse and J. Hafner, Ab Initio Molecular Dynamics for Liquid Metals, *Phys. Rev. B: Condens. Matter Mater. Phys.*, 1993, **47**, 558–561.

34 G. Kresse and J. Furthmüller, Efficiency of Ab-Initio Total Energy Calculations for Metals and Semiconductors Using a Plane-Wave Basis Set, *Comput. Mater. Sci.*, 1996, **6**, 15–50.

35 G. Kresse and J. Furthmüller, Efficient Iterative Schemes for Ab Initio Total-Energy Calculations Using a Plane-Wave Basis Set, *Phys. Rev. B: Condens. Matter Mater. Phys.*, 1996, **54**, 11169–11186.

36 P. E. Blöchl, Projector Augmented-Wave Method, *Phys. Rev. B: Condens. Matter Mater. Phys.*, 1994, **50**, 17953–17979.

37 G. Kresse and D. Joubert, From Ultrasoft Pseudopotentials to the Projector Augmented-Wave Method, *Phys. Rev. B: Condens. Matter Mater. Phys.*, 1999, **59**, 1758–1775.

38 J. P. Perdew, A. Ruzsinszky, G. I. Csonka, O. A. Vydrov, G. E. Scuseria, L. A. Constantin, X. Zhou and K. Burke, Restoring the Density-Gradient Expansion for Exchange in Solids and Surfaces, *Phys. Rev. Lett.*, 2008, **100**, 136406.





39 S. L. Dudarev, G. A. Botton, S. Y. Savrasov, C. J. Humphreys and A. P. Sutton, Electron-Energy-Loss Spectra and the Structural Stability of Nickel Oxide: An LSDA+U Study, *Phys. Rev. B: Condens. Matter Mater. Phys.*, 1998, **57**, 1505–1509.

40 G. Hautier, S. P. Ong, A. Jain, C. J. Moore and G. Ceder, Accuracy of Density Functional Theory in Predicting Formation Energies of Ternary Oxides from Binary Oxides and Its Implication on Phase Stability, *Phys. Rev. B: Condens. Matter Mater. Phys.*, 2012, **85**, 155208.

41 T. Mueller, G. Hautier, A. Jain and G. Ceder, Evaluation of Tavorite-Structured Cathode Materials for Lithium-Ion Batteries Using High-Throughput Computing, *Chem. Mater.*, 2011, **23**, 3854–3862.

42 A. Jain, S. P. Ong, G. Hautier, W. Chen, W. D. Richards, S. Dacek, S. Cholia, D. Gunter, D. Skinner, G. Ceder and K. A. Persson, The Materials Project: A Materials Genome Approach to Accelerating Materials Innovation, *APL Mater.*, 2013, **1**, 011002.

43 H. J. Monkhorst and J. D. Pack, Special Points for Brillouin-zone Integrations, *Phys. Rev. B: Solid State*, 1976, **13**, 5188–5192.

44 S. P. Ong, W. D. Richards, A. Jain, G. Hautier, M. Kocher, S. Cholia, D. Gunter, V. L. Chevrier, K. A. Persson and G. Ceder, Python Materials Genomics (Pymatgen): A Robust, Open-Source Python Library for Materials Analysis, *Comput. Mater. Sci.*, 2013, **68**, 314–319.

45 A. Jain, G. Hautier, C. J. Moore, S. Ping Ong, C. C. Fischer, T. Mueller, K. A. Persson and G. Ceder, A High-Throughput Infrastructure for Density Functional Theory Calculations, *Comput. Mater. Sci.*, 2011, **50**, 2295–2310.

46 A. V. Krukau, O. A. Vydrov, A. F. Izmaylov and G. E. Scuseria, Influence of the Exchange Screening Parameter on the Performance of Screened Hybrid Functionals, *J. Chem. Phys.*, 2006, **125**, 224106.

47 N. Biškup, J. L. Martínez, M. E. Arroyo y de Dompablo, P. Díaz-Carrasco and J. Morales, Relation between the Magnetic Properties and the Crystal and Electronic Structures of Manganese Spinels  $\text{LiNi}_{0.5}\text{Mn}_{1.5}\text{O}_4$  and  $\text{LiCu}_{0.5}\text{Mn}_{1.5}\text{O}_{4-\delta}$  ( $0 < \delta < 0.125$ ), *J. Appl. Phys.*, 2006, **100**, 093908.

48 C. J. Bradley and A. P. Cracknell, The Mathematical Theory of Symmetry in Solids : Representation Theory for Point Groups and Space Groups, *Oxford Classic Texts in the Physical Sciences*, Oxford University Press, Oxford, 2010.

49 A. M. Ganose, A. J. Jackson and D. O. Scanlon, Sumo: Command-line Tools for Plotting and Analysis of Periodic \*ab Initio\* Calculations, *J. Open Source Softw.*, 2018, **3**, 717.

50 C. G. Van de Walle and J. Neugebauer, First-Principles Calculations for Defects and Impurities: Applications to III-nitrides, *J. Appl. Phys.*, 2004, **95**, 3851–3879.

51 S. Kavanagh, Defect Oriented Python Environment Distribution, <https://github.com/SMTG-UCL/doped>.

52 D. Broberg, B. Medasani, N. E. Zimmermann, G. Yu, A. Canning, M. Haranczyk, M. Asta and G. Hautier, PyCDT: A Python Toolkit for Modeling Point Defects in Semiconductors and Insulators, *Comput. Phys. Commun.*, 2018, **226**, 165–179.

53 I. Mosquera-Lois, S. R. Kavanagh, A. Walsh and D. O. Scanlon, ShakeNBreak: Navigating the Defect Configurational Landscape, *J. Open Source Softw.*, 2022, **7**, 4817.

54 I. Mosquera-Lois, S. R. Kavanagh, A. Walsh and D. O. Scanlon, Identifying the Ground State Structures of Point Defects in Solids, *npj Comput. Mater.*, 2023, **9**, 25.

55 I. Mosquera-Lois and S. R. Kavanagh, In Search of Hidden Defects, *Matter*, 2021, **4**, 2602–2605.

56 G. Henkelman and H. Jónsson, Improved Tangent Estimate in the Nudged Elastic Band Method for Finding Minimum Energy Paths and Saddle Points, *J. Chem. Phys.*, 2000, **113**, 9978–9985.

57 G. Henkelman, B. P. Uberuaga and H. Jónsson, A Climbing Image Nudged Elastic Band Method for Finding Saddle Points and Minimum Energy Paths, *J. Chem. Phys.*, 2000, **113**, 9901–9904.

58 K. Momma and F. Izumi, VESTA: A Three-Dimensional Visualization System for Electronic and Structural Analysis, *J. Appl. Crystallogr.*, 2008, **41**, 653–658.

59 K. Hoang and M. D. Johannes, Defect Physics in Complex Energy Materials, *J. Phys.: Condens. Matter*, 2018, **30**, 293001.

60 C. Freysoldt, J. Neugebauer and C. G. Van de Walle, Fully Ab Initio Finite-Size Corrections for Charged-Defect Supercell Calculations, *Phys. Rev. Lett.*, 2009, **102**, 016402.

61 R. A. Lunt, A. J. Jackson and A. Walsh, Dielectric Response of  $\text{Fe}_2\text{O}_3$  Crystals and Thin Films, *Chem. Phys. Lett.*, 2013, **586**, 67–69.

62 X. Xu, S. Deng, H. Wang, J. Liu and H. Yan, Research Progress in Improving the Cycling Stability of High-Voltage  $\text{LiNi}_{0.5}\text{Mn}_{1.5}\text{O}_4$  Cathode in Lithium-Ion Battery, *Nano-Micro Lett.*, 2017, **9**, 22.

63 J. Buckeridge, D. Scanlon, A. Walsh and C. Catlow, Automated Procedure to Determine the Thermodynamic Stability of a Material and the Range of Chemical Potentials Necessary for Its Formation Relative to Competing Phases and Compounds, *Comput. Phys. Commun.*, 2014, **185**, 330–338.

64 J. Buckeridge, *Chemical Potential Limits Analysis Program*, <https://github.com/jbuckeridge/cplap>.

65 A. Jain, G. Hautier, S. Ong, C. Moore, C. Fischer, K. Persson and G. Ceder, Formation Enthalpies by Mixing GGA and GGA + U Calculations, *Phys. Rev. B: Condens. Matter Mater. Phys.*, 2011, **84**, 045115.

66 S. P. Ong, L. Wang, B. Kang and G. Ceder, Li-Fe-P-O<sub>2</sub> Phase Diagram from First Principles Calculations, *Chem. Mater.*, 2008, **20**, 1798–1807.

67 V. Massarotti, D. Capsoni, M. Bini, G. Chiodelli, C. Azzoni, M. Mozzati and A. Palleari, Electric and Magnetic Properties of  $\text{LiMn}_2\text{O}_4$ - and  $\text{Li}_2\text{MnO}_3$ -Type Oxides, *J. Solid State Chem.*, 1997, **131**, 94–100.

68 W.-W. Liu, D. Wang, Z. Wang, J. Deng, W.-M. Lau and Y. Zhang, Influence of Magnetic Ordering and Jahn–Teller

Distortion on the Lithiation Process of  $\text{LiMn}_2\text{O}_4$ , *Phys. Chem. Chem. Phys.*, 2017, **19**, 6481–6486.

69 Z. Yao, S. Kim, J. He, V. I. Hegde and C. Wolverton, Interplay of Cation and Anion Redox in  $\text{Li}_4\text{Mn}_2\text{O}_5$  Cathode Material and Prediction of Improved  $\text{Li}_4(\text{Mn,M})_2\text{O}_5$  Electrodes for Li-ion Batteries, *Sci. Adv.*, 2018, **4**, eaao6754.

70 Z. H. Wang, D. Y. Geng, W. J. Hu, W. J. Ren and Z. D. Zhang, Magnetic Properties and Exchange Bias in  $\text{Mn}_2\text{O}_3/\text{Mn}_3\text{O}_4$  Nanoclusters, *J. Appl. Phys.*, 2009, **105**, 07AV315.

71 B. A. Frandsen and S. J. L. Billinge, Magnetic Structure Determination from the Magnetic Pair Distribution Function (mPDF): Ground State of  $\text{MnO}$ , *Acta Crystallogr., Sect. A: Found. Adv.*, 2015, **71**, 325–334.

72 S. v. Ivanova, E. Zhecheva, D. Nihtianova and R. Stoyanova, Nano-Domain Structure of  $\text{Li}_4\text{Mn}_5\text{O}_{12}$  Spinel, *J. Mater. Sci.*, 2011, **46**, 7098–7105.

73 I. Davidson, J. Greedan, U. Von Sacken, C. Michal and W. McKinnon, Short Range and Long Range Magnetic Order in 1T- $\text{Li}_2\text{NiO}_2$ , *J. Solid State Chem.*, 1993, **105**, 410–416.

74 K. Kang, C.-H. Chen, B. J. Hwang and G. Ceder, Synthesis, Electrochemical Properties, and Phase Stability of  $\text{Li}_2\text{NiO}_2$  with the Immm Structure, *Chem. Mater.*, 2004, **16**, 2685–2690.

75 V. Bianchi, D. Caurant, N. Baffier, C. Belhomme, E. Chappel, G. Chouteau, S. Bach, J. Pereira-Ramos, A. Sulpice and P. Wilmann, Synthesis, Structural Characterization and Magnetic Properties of Quas stoichiometric  $\text{LiNiO}_2$ , *Solid State Ionics*, 2001, **140**, 1–17.

76 A. Kuwabara, C. A. J. Fisher, Y. H. Ikuhara, H. Moriwake, H. Oki and Y. Ikuhara, The Influence of Charge Ordering on the Phase Stability of Spinel  $\text{LiNi}_2\text{O}_4$ , *RSC Adv.*, 2012, **2**, 12940–12948.

77 K. Hoang and M. Johannes, Tailoring Native Defects in  $\text{LiFePO}_4$ : Insights from First-Principles Calculations, *Chem. Mater.*, 2011, **23**, 3003–3013.

78 A. Squires, D. Scanlon and B. Morgan, Py-Sc-Fermi: Self-Consistent Fermi Energies and Defect Concentrations from Electronic Structure Calculations, *J. Open Source Softw.*, 2023, **8**, 4962.

79 J. Buckeridge, Equilibrium Point Defect and Charge Carrier Concentrations in a Material Determined through Calculation of the Self-Consistent Fermi Energy, *Comput. Phys. Commun.*, 2019, **244**, 329–342.

80 C. Kittel and H. Kroemer, *Thermal Physics*, American Association of Physics Teachers, 1998.

81 D. W. Davies, B. J. Morgan, D. O. Scanlon and A. Walsh, Low-Cost Descriptors of Electrostatic and Electronic Contributions to Anion Redox Activity in Batteries, *IOP SciNotes*, 2020, **1**, 024805.

82 D. O. Scanlon, C. W. Dunnill, J. Buckeridge, S. A. Shevlin, A. J. Logsdail, S. M. Woodley, C. R. A. Catlow, M. J. Powell, R. G. Palgrave, I. P. Parkin, G. W. Watson, T. W. Keal, P. Sherwood, A. Walsh and A. A. Sokol, Band Alignment of Rutile and Anatase  $\text{TiO}_2$ , *Nat. Mater.*, 2013, **12**, 798–801.

83 D. Krasikov and I. Sankin, Defect Interactions and the Role of Complexes in the CdTe Solar Cell Absorber, *J. Mater. Chem. A*, 2017, **5**, 3503–3513.

84 M. K. Horton, J. H. Montoya, M. Liu and K. A. Persson, High-Throughput Prediction of the Ground-State Collinear Magnetic Order of Inorganic Materials Using Density Functional Theory, *npj Comput. Mater.*, 2019, **5**, 64.

85 A. Chakraborty, S. Kunnikuruvan, S. Kumar, B. Markovsky, D. Aurbach, M. Dixit and D. T. Major, Layered Cathode Materials for Lithium-Ion Batteries: Review of Computational Studies on  $\text{LiNi}_{1-x-y}\text{Co}_x\text{Mn}_y\text{O}_2$  and  $\text{LiNi}_{1-x-y}\text{Co}_x\text{Al}_y\text{O}_2$ , *Chem. Mater.*, 2020, **32**, 915–952.

86 K. Hoang, Understanding the Electronic and Ionic Conduction and Lithium Over-Stoichiometry in  $\text{LiMn}_2\text{O}_4$  Spinel, *J. Mater. Chem. A*, 2014, **2**, 18271–18280.

87 W. H. Kan, S. Kuppan, L. Cheng, M. Doeff, J. Nanda, A. Huq and G. Chen, Crystal Chemistry and Electrochemistry of  $\text{Li}_x\text{Mn}_{1.5}\text{Ni}_{0.5}\text{O}_4$  Solid Solution Cathode Materials, *Chem. Mater.*, 2017, **29**, 6818–6828.

88 B. Aktekin, F. Massel, M. Ahmadi, M. Valvo, M. Hahlin, W. Zipprich, F. Marzano, L. Duda, R. Younesi, K. Edström and D. Brandell, How Mn/Ni Ordering Controls Electrochemical Performance in High-Voltage Spinel  $\text{LiNi}_{0.44}\text{Mn}_{1.56}\text{O}_4$  with Fixed Oxygen Content, *ACS Appl. Energy Mater.*, 2020, **3**, 6001–6013.

89 H. Liu, J. Zhou, L. Zhang, Z. Hu, C. Kuo, J. Li, Y. Wang, L. H. Tjeng, T.-W. Pi, A. Tanaka, L. Song, J.-Q. Wang and S. Zhang, Insight into the Role of Metal–Oxygen Bond and O 2p Hole in High-Voltage Cathode  $\text{LiNi}_x\text{Mn}_{2-x}\text{O}_4$ , *J. Phys. Chem. C*, 2017, **121**, 16079–16087.

90 H. Ryoo, S.-G. Lee, J.-G. Kim and S.-Y. Chung, Effect of Chemical Bonding Characteristics on Ordering Structure in Li Spinel Oxides, *Adv. Funct. Mater.*, 2019, **29**, 1805972.

91 J. A. Santana, J. Kim, P. R. C. Kent and F. A. Reboredo, Successes and Failures of Hubbard-corrected Density Functional Theory: The Case of Mg Doped  $\text{LiCoO}_2$ , *J. Chem. Phys.*, 2014, **141**, 164706.

92 M. M. S. Sanad, H. A. Abdellatif, E. M. Elnaggar, G. M. El-Kady and M. M. Rashad, Understanding Structural, Optical, Magnetic and Electrical Performances of Fe- or Co-substituted Spinel  $\text{LiMn}_{1.5}\text{Ni}_{0.5}\text{O}_4$  Cathode Materials, *Appl. Phys. A*, 2019, **125**, 139.

93 M. Raja, S. Mahanty and R. Basu, Influence of S and Ni Co-Doping on Structure, Band Gap and Electrochemical Properties of Lithium Manganese Oxide Synthesized by Soft Chemical Method, *J. Power Sources*, 2009, **192**, 618–626.

94 S. K. Radha, W. R. L. Lambrecht, B. Cunningham, M. Grüning, D. Pashov and M. van Schilfgaarde, Optical Response and Band Structure of  $\text{LiCoO}_2$  Including Electron-Hole Interaction Effects, *Phys. Rev. B*, 2021, **104**, 115120.

95 S. R. Kavanagh, C. N. Savory, S. M. Liga, G. Konstantatos, A. Walsh and D. O. Scanlon, Frenkel Excitons in Vacancy-Ordered Titanium Halide Perovskites ( $\text{Cs}_2\text{TiX}_6$ ), *J. Phys. Chem. Lett.*, 2022, **13**, 10965–10975.





96 J. Cen, B. Zhu and D. Scanlon, *Exploring Battery Cathode Materials in the Li-Ni-O Phase Diagrams Using Structure Prediction*, 2022, DOI: [10.26434/chemrxiv-2022-gdmdh-v2](https://doi.org/10.26434/chemrxiv-2022-gdmdh-v2).

97 K. Hoang, Defect Physics, Delithiation Mechanism, and Electronic and Ionic Conduction in Layered Lithium Manganese Oxide Cathode Materials, *Phys. Rev. Appl.*, 2015, **3**, 024013.

98 M. Burbano, D. O. Scanlon and G. W. Watson, Sources of Conductivity and Doping Limits in CdO from Hybrid Density Functional Theory, *J. Am. Chem. Soc.*, 2011, **133**, 15065–15072.

99 P. Stüble, V. Mereacre, H. Geßwein and J. R. Binder, On the Composition of  $\text{LiNi}_{0.5}\text{Mn}_{1.5}\text{O}_4$  Cathode Active Materials, *Adv. Energy Mater.*, 2023, 2203778.

100 W. Tang, E. Sanville and G. Henkelman, A Grid-Based Bader Analysis Algorithm without Lattice Bias, *J. Phys.: Condens. Matter*, 2009, **21**, 084204.

101 G. Henkelman, A. Arnaldsson and H. Jónsson, A Fast and Robust Algorithm for Bader Decomposition of Charge Density, *Comput. Mater. Sci.*, 2006, **36**, 354–360.

102 Z. Moorhead-Rosenberg, K. R. Chemelewski, J. B. Goodenough and A. Manthiram, Magnetic Measurements as a Viable Tool to Assess the Relative Degrees of Cation Ordering and  $\text{Mn}^{3+}$  Content in Doped  $\text{LiMn}_{1.5}\text{Ni}_{0.5}\text{O}_4$  Spinel Cathodes, *J. Mater. Chem. A*, 2013, **1**, 10745–10752.

103 C. E. Housecroft, *Inorganic Chemistry*, Pearson, Harlow, England, 5th edn, 2018.

104 R. D. Shannon, Revised Effective Ionic Radii and Systematic Studies of Interatomic Distances in Halides and Chalcogenides, *Acta Crystallogr., Sect. A: Found. Adv.*, 1976, **32**, 751–767.

105 Y. Han, Y.-S. Jiang, Y. Xia, L. Deng, L.-F. Que, F.-D. Yu and Z.-B. Wang, Suppressed Phase Separation in Spinel  $\text{LiNi}_{0.5}\text{Mn}_{1.5}\text{O}_4$  Cathode via Interstitial Sites Modulation, *Nano Energy*, 2022, **91**, 106636.

106 E. Hu, S.-M. Bak, Y. Liu, J. Liu, X. Yu, Y.-N. Zhou, J. Zhou, P. Khalifah, K. Ariyoshi, K.-W. Nam and X.-Q. Yang, Utilizing Environmental Friendly Iron as a Substitution Element in Spinel Structured Cathode Materials for Safer High Energy Lithium-Ion Batteries, *Adv. Energy Mater.*, 2016, **6**, 1501662.

107 A. Y. Toukmaji and J. A. Board, Ewald Summation Techniques in Perspective: A Survey, *Comput. Phys. Commun.*, 1996, **95**, 73–92.

108 J. Coutinho, V. P. Markevich and A. R. Peaker, Characterisation of Negative-U Defects in Semiconductors, *J. Phys.: Condens. Matter*, 2020, **32**, 323001.

109 J. Qu, V. Stevanović, E. Ertekin and P. Gorai, Doping by Design: Finding New n-Type Dopeable  $\text{ABX}_4$  Zintl Phases for Thermoelectrics, *J. Mater. Chem. A*, 2020, **8**, 25306–25315.

110 D. O. Scanlon, Defect Engineering of  $\text{BaSnO}_3$  for High-Performance Transparent Conducting Oxide Applications, *Phys. Rev. B: Condens. Matter Mater. Phys.*, 2013, **87**, 161201.

111 J. Buckeridge, C. R. A. Catlow, M. R. Farrow, A. J. Logsdail, D. O. Scanlon, T. W. Keal, P. Sherwood, S. M. Woodley, A. A. Sokol and A. Walsh, Deep vs. Shallow Nature of Oxygen Vacancies and Consequent N-Type Carrier Concentrations in Transparent Conducting Oxides, *Phys. Rev. Mater.*, 2018, **2**, 054604.

112 X. Ma, B. Kang and G. Ceder, High Rate Micron-Sized Ordered  $\text{LiNi}_{0.5}\text{Mn}_{1.5}\text{O}_4$ , *J. Electrochem. Soc.*, 2010, **157**, A925.

113 B. Xu and S. Meng, Factors Affecting Li Mobility in Spinel  $\text{LiMn}_2\text{O}_4$ —A First-Principles Study by GGA and GGA+U Methods, *J. Power Sources*, 2010, **195**, 4971–4976.

114 S. R. Kavanagh, D. O. Scanlon, A. Walsh and C. Freysoldt, Impact of Metastable Defect Structures on Carrier Recombination in Solar Cells, *Faraday Discuss.*, 2022, **239**, 339–356.

115 A. A. Sokol, S. A. French, S. T. Bromley, C. R. A. Catlow, H. J. J. van Dam and P. Sherwood, Point Defects in  $\text{ZnO}$ , *Faraday Discuss.*, 2007, **134**, 267–282.

116 D. O. Scanlon and G. W. Watson, On the Possibility of P-Type  $\text{SnO}_2$ , *J. Mater. Chem.*, 2012, **22**, 25236–25245.

117 G. Liu, Y. Li and B. Wang, Importance of Cooling Speed on Rapid Synthesis of  $\text{LiNi}_{0.5}\text{Mn}_{1.5}\text{O}_4$  by a Solution Combustion Synthesis Method, *Int. J. Electrochem. Sci.*, 2015, **10**, 3124–3135.

118 J. H. Kim, J.-W. Jung, S.-H. Cho, I.-D. Kim, Y. C. Park, D.-H. Seo and H.-S. Kim, Investigation of Ordering on Oxygen-Deficient  $\text{LiNi}_{0.5}\text{Mn}_{1.5}\text{O}_{4-\delta}$  Thin Films for Boosting Electrochemical Performance in All-Solid-State Thin-Film Batteries, *Small*, 2022, **18**, 2201134.

119 H. Shiiba, N. Zettsu, S. Kida, D.-w. Kim and K. Teshima, Impact of Trace Extrinsic Defect Formation on the Local Symmetry Transition in Spinel  $\text{LiNi}_{0.5}\text{Mn}_{1.5}\text{O}_{4-\delta}$  Systems and Their Electrochemical Characteristics, *J. Mater. Chem. A*, 2018, **6**, 22749–22757.

120 X. He, Y. Zhu and Y. Mo, Origin of Fast Ion Diffusion in Super-Ionic Conductors, *Nat. Commun.*, 2017, **8**, 15893.

121 K. Sasaki and J. Maier, Low-Temperature Defect Chemistry of Oxides. I. General Aspects and Numerical Calculations, *J. Appl. Phys.*, 1999, **86**, 5422–5433.

122 A. G. Squires, D. O. Scanlon and B. J. Morgan, Native Defects and Their Doping Response in the Lithium Solid Electrolyte  $\text{Li}_7\text{La}_3\text{Zr}_2\text{O}_{12}$ , *Chem. Mater.*, 2020, **32**, 1876–1886.

123 A. Squires, J. M. Dean and B. J. Morgan, *Aliovalent Doping Response and Impact on Ionic Conductivity in the Antiperovskite Solid Electrolyte  $\text{Li}_3\text{OCl}$* , 2021, DOI: [10.33774/chemrxiv-2021-zvwhh-v2](https://doi.org/10.33774/chemrxiv-2021-zvwhh-v2).